Fall 2018

Structural and Aerodynamic Design, Procedure and Analysis of a Small V-shaped Vertical Axis Wind Turbine

Odari J. Whyte

Follow this and additional works at: https://digitalcommons.georgiasouthern.edu/etd

 Part of the Computer-Aided Engineering and Design Commons, Electro-Mechanical Systems Commons, Energy Systems Commons, Mechanics of Materials Commons, Other Engineering Commons, and the Other Engineering Science and Materials Commons

STRUCTURAL AND AERODYNAMIC DESIGN, PROCEDURE AND ANALYSIS OF A

SMALL V-SHAPED VERTICAL AXIS WIND TURBINE ROTOR

by

ODARI JASON WHYTE

(Under the Direction of Mosfequr Rahman)

ABSTRACT

Over the last two decades there has been a renewed interest in Vertical Axis Wind Turbines. This turbine configuration though unpopular for large-scale generation has found a niche market in the way of offshore energy harvesting. However, offshore wind has its challenges. In this thesis a detailed comprehensive study of a proposed V-shaped vertical axis turbine rotor is performed in order to examine its structural and aerodynamic characteristics. The design met and exceeded the safety parameters establish for test bed operation, showing a factor of safety of 1.87 with regard to fatigue stress response. A satisfactory fatigue stress design life was also achieved. Both experimental and numerical aerodynamic data have relatively good agreement achieving an overall maximum power coefficient of 0.2589 numerically and 0.251 experimentally.

INDEX WORDS: Wind energy, Vertical axis wind turbine, VAWT, V-shaped, Structural, Design, Rotor design, Renewable energy, Darrieus turbine, CFD.

STRUCTURAL AND AERODYNAMIC DESIGN, PROCEDURE AND ANALYSIS OF A

SMALL V-SHAPED VERTICAL AXIS WIND TURBINE ROTOR

by

ODARI JASON WHYTE

B.S., Georgia Southern University, 2013

A Thesis Submitted to the Graduate Faculty of Georgia Southern University in Partial

Fulfillment of the Requirements for the Degree

MASTER OF SCIENCE

STATESBORO, GEORGIA

STRUCTURAL AND AERODYNAMIC DESIGN, PROCEDURE AND ANALYSIS OF A

SMALL V-SHAPED VERTICAL AXIS WIND TURBINE ROTOR

by

ODARI JASON WHYTE

Major Professor: Mosfequr Rahman
Committee: Valentin Soloiu
                   Marcell Ilie

Electronic Version Approved:

December 2018

DEDICATION

This work is dedicated to my parents Merlin and Vincent Whyte, extended family and friends who support me in every effort and encouraged me to keep moving forward. I could not have accomplished this without you all.

ACKNOWLEDGMENTS

I would like to acknowledge Dr. Mosfequr Rahman for his guidance and direction throughout my research in his wind energy laboratory. I want to thank Dr. Valentin Soloiu and Dr. Marcel Ilie for their guidance in this work and for taking time to be a part of my thesis committee along with reviewing this work. My thanks are also extended to the Allen E. Paulson College of Engineering and I.T. as well as the Brian Lang with University Housing at Georgia Southern University, for providing me with the knowledge and skills necessary to accomplish this work.

TABLE OF CONTENTS

LIST OF FIGURES

LIST OF TABLES

CHAPTER 1

INTRODUCTION

1.1 Purpose of the Study

Globally, our demand for energy is ever-increasing while the sources we have depended on for the last few centuries become scarcer and the environmental problems they cause loom ever larger. In seeking new renewable and/or carbon-free alternative energy sources, we are faced with challenges in human health risks, cost and economics, political as well as social education about alternatives and the mismatch between the supply and demand that these alternatives present. According to (Mahesh and Sandhu 2015), the potential candidates range from solar power, to harnessing the tides, to wind, to nuclear power and beyond. The question remains, however, which of these alternative sources would be the best choice to replace coal and oil for our future energy needs?

Solar and wind energy to date, has proven to be the most common and attractive alternative energy producing mediums available. However, the unpredictability of nature has been the greatest obstacle standing between these proposals becoming major players in quelling the concerns in the pursuit of sustainable energy production. Both solar and wind energy are inexhaustible and help to reduce cost of adding renewables to most energy portfolios. The ability to properly size these systems based on the immediate demand also help to make them even more attractive (Mahesh and Sandhu 2015).

1.2 Economic Assessment

From the outset of project development, investors in wind energy have relatively certain knowledge of the plant's lifetime cost of wind energy. This is because a wind energy project's

installed costs and mean wind speed are known early on, and wind generation generally has low variable costs, zero fuel cost, and no carbon emission costs. Even with these inherent characteristics, there are, however, wide variations in the cost of wind energy from project to project, within a country, and internationally. The variability of the all-in cost of wind energy, however, may still be a barrier for increased deployment of wind energy across the globe. (Schwabe, Lensink and Hand 2011).

In the past 30 years, onshore wind installed costs have declined significantly, according to IRENAs database of onshore wind power project costs from 1983-2016. The estimated global weighted average fall in total installed cost of wind farms between 1983 and 2017 was 70%, as costs fell from USD 4 880 to USD 1 477/kW, (Figure 1.1). This represents a learning curve of 9% for total installed costs for every time installed capacity doubled, worldwide (Ilas, et al. 2018).
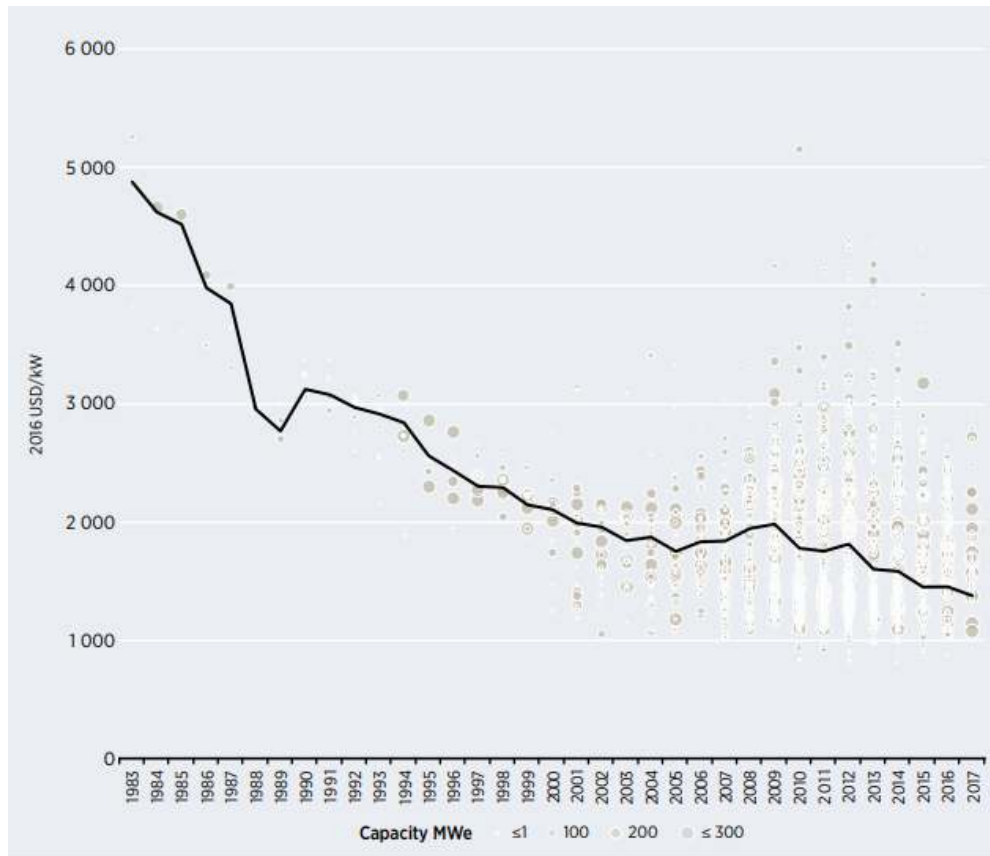
Figure 1.1. Total installed costs of onshore wind projects and global weighted average, 1983-2017 (Ilas, et al. 2018).

The start date for first commercial install of turbines varies, based on country. This leads to a complicated comparative analysis. Despite this, the installed cost reductions of different countries show a range of declines, from 30% (in the United Kingdom) to 68% (in the United States), and it is clear from comparison on an installed cost basis, that a shift in deployment to the most competitive countries has resulted in a larger global weighted average cost reduction than has been seen in any one country (Ilas, et al. 2018).

In proportion to this growth, we have now crossed a threshold in technology where 15 rotations of a single 8MW wind turbine can power a moderately sized home for an entire day (Vaughan 2017). These mammoth machines are ten times more powerful that was previously achieved and are taller than the Empire State Building. It is innovations like these that are making

wind energy one of the cheapest sources of energy in most of the United States, since the fuel is free, and the cost of manufacturing, operation and maintenance is only getting cheaper. There is a boundless supply of wind here in the U.S., as the Energy Department notes that North Dakota, Wyoming and Montana alone could supply more that 80% of the country's energy needs (Elliot, Wendell and Gower 1991). Wind energy harnessing is such a success that it has become one of the fastest growing industries in America, with 4 states already acquiring at least 30% of their energy from wind (Kusnetz 2018). The industry is creating thousands of jobs, and is already on par with the total employment of the coal-mining industry, and is projected to double in the coming ten years. Manufacturing, construction and maintenance, are just some of the jobs this industry has opened, from which the average salary is around USD$53,000 (Bureau of Labor Statistics 2018).

1.3 The Rise of Vertical Axis Wind Turbines

Offshore wind resources were completely untapped in the U.S., until recently. According to the EIA, May 2017, until late 2016, all U.S. wind capacity was on land. The first U.S. offshore wind project, Block Island Wind Farm, began commercial operation off the coast of Rhode Island in December 2016 with a generating capacity of 29.3 MW (Beckford 2017).

Designing turbines specifically for offshore use is still one of the most important bottlenecks in the construction of wind farms at sea. Most of the turbines going offshore at the moment are based on onshore turbine design (Li and Wang 2011). There are several variables working against conventional wind turbine designs once they are exported to offshore use. For example, offshore areas that present ideal wind conditions sometimes pose issues, where structurally interfacing turbine towers with the seafloor is not feasible, thus leading to the use of floating turbines. These floating structures then open up a myriad of new issues that come with floating structures, such as, the stability of the structure, having to accommodate for added stresses,

highly unsafe maintenance conditions, and the associated cost of planning around these various safety issues. This is where VAWTs become relevant.

1.4 The Vertical Axis Turbine Niche

A vertical-axis wind turbine (VAWT) rotor configuration offers a potential transformative technology solution that significantly lowers COE for offshore wind due to its inherent advantages for the offshore market (Owens and Griffith, Aeroelastic Stability Investigations for Large-scale Vertical Axis Wind Turbines 2014). The arrangement of a VAWT places the integral components at the structures base, giving it the potential to reduce costs associated with servicing and support structure requirements (Owens and Griffith, Aeroelastic Stability Investigations for Large-scale Vertical Axis Wind Turbines 2014). Another area in which VAWTs shine is in energy density of wind farms. Horizontal axis wind turbines farms have shown an energy density of between 2-3 watts of power per square meter of land, however, in summer of 2010, it was confirmed that power densities an order of magnitude greater can potentially be achieved by arranging VAWTs in layouts that enable them to extract energy from adjacent wakes, in fact, VAWT farms show a potential production of 30 W per square meter (Dabiri 2011). This discovery could potentially solve one of the major issues with Wind energy which is, its massive need for space.

1.5 Contribution to Science

In 2009 the Energy Technologies Institute (ETI) commissioned the NOVA (Novel Offshore Vertical Axis) project, a £2.8M feasibility project to develop the design of a novel 10 MW offshore VAWT based on the novel V-shape rotor (Parsons, et al. 2011). Through detailed technological, economic and environmental assessments, a consortium that included industrial partners, developed a preliminary design over a period of 18 months, illustrated in Figure 1.2.

Figure 1.3 displays a photograph of a 5 kW prototype device developed by David Sharpe (Sharpe 2011) and Wind Power Ltd prior to the NOVA project, undergoing tests at Cranfield University (Wang, et al. 2016).
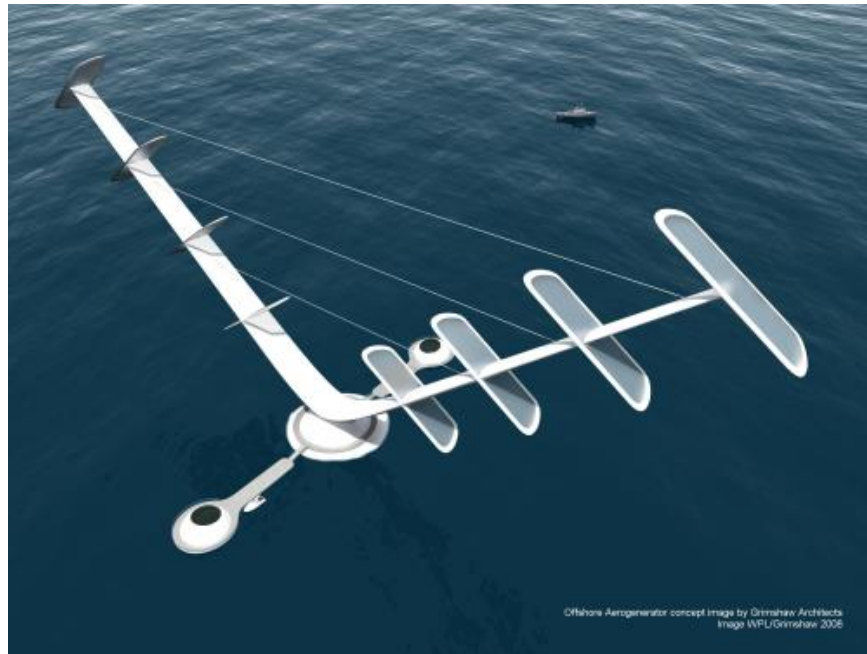
Figure 1.2. Concept design of NOVA 10MW wind turbine (Sharpe 2011).

Figure 1.3. 5 kW prototype device developed by Wind Power Ltd (Wang, et al. 2016).

In light of these previous endeavors, there are several avenues available to extend the body of knowledge as it currently stands. Firstly, there have been few efforts made to assess the effects of a conventional HAWT blade design without the addition of sectioned aero-foil/hydrofoil sections to the blade, on a V-shaped design. Secondly, a great deal of the existing body of research seems to be more focused on the structural longevity of the system rather than the aerodynamic capabilities, and lastly, knowledge of the effects of inclination angle, as well as the application of more than two blades and their effects on power production are limited.

1.6 Research Scope

In this thesis a detailed comprehensive study of a proposed V-shaped turbine rotor is performed in order to examine its structural and aerodynamic characteristics. The structural portion of this study will seek to determine between 3 different blade configurations where, root design, overall blade geometry and structural failure features will be analyzed. After this the blade design that proves to be the most structurally sound will then be optimized for experimental and numerical aerodynamic testing purposes. In the aerodynamic portion of this study, the selected blade geometry from the structural analysis is applied to eight different rotor designs and analyzed with wind tunnel testing and numerical simulations. 3D static Computational Fluid Dynamics (CFD) analysis using the ANSYS CFX platform is used to determine the effects of inclination angle, wind speed and blade twist angle on power performance. From the numerical study the 4 best performing turbine rotors are 3D printed and used for wind tunnel experimentation. Experiments are conducted to find reactional torque and rotations per minute (RPM) from which turbine efficiencies are calculated. The main efforts of this research are as follows:

- Determine a structurally capable blade geometry.
- Structurally refine blade geometry for testing purposes.
- Investigate the effect of inclination angle on a V-shaped rotor.
- Create a repeatable model for the experimental testing of vertical axis turbines.
- Numerically and experimentally assess the power efficiency of a V-shaped wind turbine rotor.
- Institute an improved three-dimensional static aerodynamic model for wind turbine simulation in the Georgia Southern University Wind Energy Lab.

- Design method for the investigation of the structural aspects of wind turbines in the current lab.

It is hypothesized that the proposed rotor design will produce equivalent energy as a similarly sized conventional straight-bladed or helical Darrieus rotor. Also, this research will seek to improve the methods of aerodynamic analysis as well as institute a structural design method for wind turbine blades in the Georgia Southern University Wind Energy Lab.

1.7 Criteria for Success

In order for the experiment to be successful, it must be proven that a proposed rotor configuration can achieve coefficient of power values either numerically and/or experimentally that is comparable to those of traditional straight-bladed H-type Darrieus turbines. Otherwise a minimum power performance power performance of around 0.12 (which is the maximum efficiency of a Savonius rotor) corroborated both numerically and experimentally. For structural results, a minimum Factor of Safety of 1.5 for all assessed Structural criteria must be achieved. It must be determined if the rotor can withstand a 50 years storm condition as dictated by the International Electro-technical Commission (IEC) and finally institute a safe experimental testing is to be achieved.

1.8 Outline of the Thesis

The outline of this present work is organized as follows. Chapter 2 entails a literature review of past research efforts in this field, and current VAWT capabilities. In this section papers are reviewed and detailed based on their contribution to the conversation about V-shaped rotor technology. Methods for experimentation and numerical analysis are discussed.

Chapter 3 details the methodology, both numerical and experimental, used in this analysis. The best method for the proposed wind turbine is discussed and chosen, based on the required results. Mathematical expressions which describes the turbine performance and methodology for ANSYS FEA software is detailed as well as experimental method.

Covered in chapter 4 is the performance of the proposed wind turbine rotor design. The discussion in this chapter is addressed in two sections the discussion of structural results and the subsequently the aerodynamic results. The aerodynamic results are further broken into 2 parts where the experimental vs numerical results are addressed.

Finally a summary of the results found by this research is detailed in chapter 5.

CHAPTER 2

LITERATURE REVIEW

2.1 VAWT Overview

There are two main types of rotors that fall under vertical axis wind turbines, they are the Savonius type, which is drag based and the Darrieus type which is lift based. Depicted in Figure 2.1 is the Savonius rotor (left) and the Darrieus rotor (right) (Osea and M.Roslan 2017).
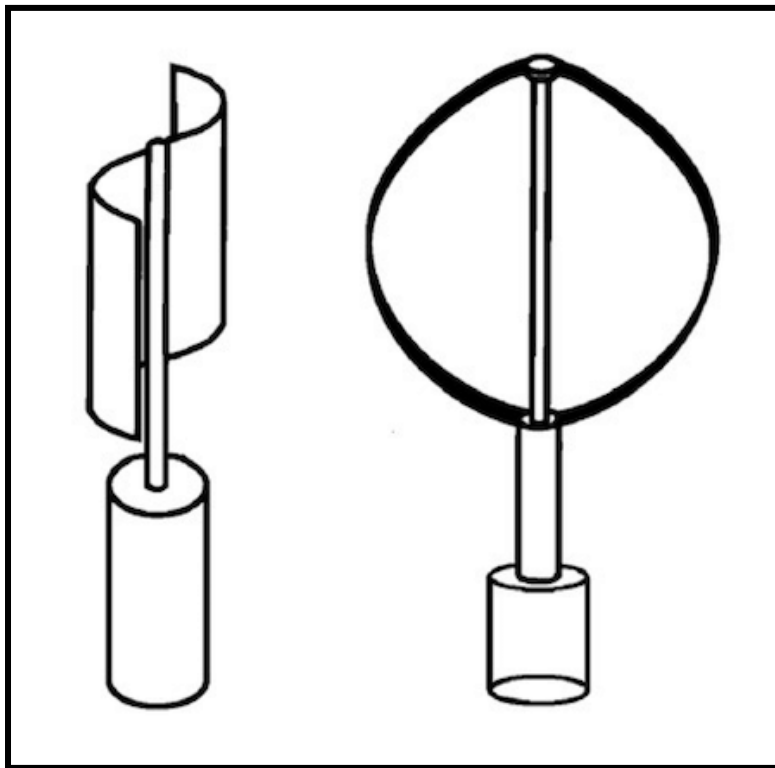
Figure 2.1. Types of VAWT (Savonius and Darrieus types) (Osea and M.Roslan 2017).

There are many advantages to having a VAWT design over the conventional HAWT. Vertical axis turbines are:

- Omni-directional, and generally do not need to track the wind, in order to collect power.

- VAWT anatomy, allows for gearboxes to be replaced and maintained much simpler and more efficiently than horizontal axis wind turbines. This is because the gearbox is accessible at ground level, so that that no cranes or other large equipment are needed. This in-turn reduces costs and impact on the environment.

- Where suitable some VAWT designs can be erected with the use screw pile foundations, which are fully recyclable. These help to reduce the road transport of concrete and other building materials which offset the carbon cost of installation.

- As was stated earlier, VAWTs can be grouped more closely in wind farms, increasing the generated power per unit area of land (Dabiri 2011).

- VAWTs can be integrated into existing HAWT wind farms below the existing HAWTs; this can supplement the power output of the existing farm (Xie, et al. 2016).

- VAWTs are much more receptive to turbulent flow thus enabling them to be erected in more urban areas.

2.2 Savonius Turbine Research

Savonius turbines are drag-based designs and the body of knowledge has progressed substantially over the past 30 years. Normal drag force (F_n) acts perpendicular to the blade wall and tangential drag force (F_t) acts along the tangential direction of each blade (Bashar, Rahman, and Khan, 2013). The schematic diagram of the Savonius rotor cross-section with the components of drag forces on each blade is illustrated in Figure 2.2
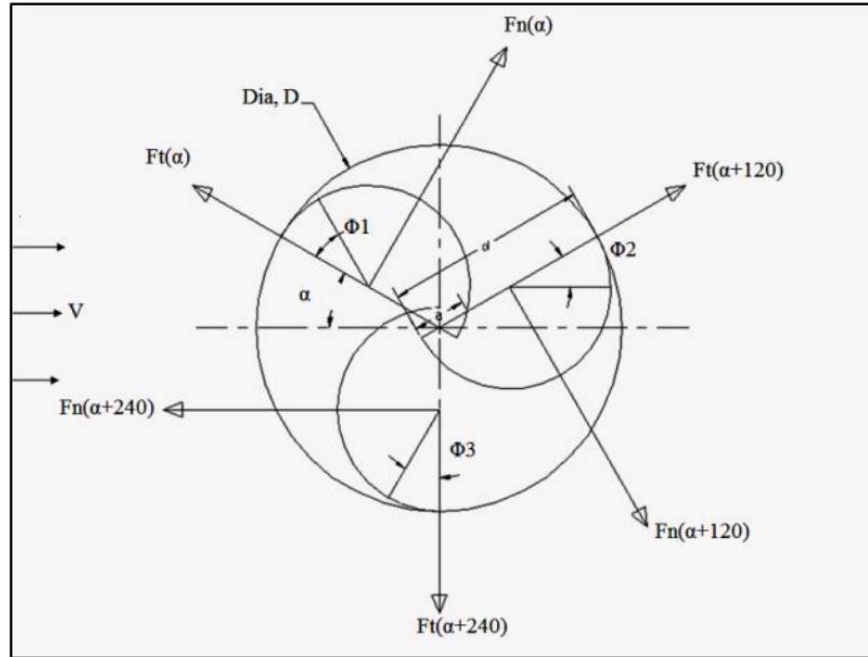
Figure 2.2. Schematic of the drag force components on model cross-section (Bashar, Rahman and Khan 2014).

The introduction of several new design characteristics have led to improvements in power performance, aesthetics, and the introduction of methods to smooth out variable and erratic behaviors of these rotors. A summary of such results can be viewed in Table 2.1 (Salyers 2016). The information in Table 2.1, describes the advancements the body of research has made over the most recent years.

Researcher(s)	Studied	Findings	Figure
Wenehenubun et al. (2015)	Influence of increasing number of blades on Savonius rotor	4 blade turbine performs best at low tip-speed ratios, 3 blade at higher tip-speed ratios	
Ghatage et al. (2012)	Effects of twisted rotors	Twisting the blades enhanced efficiency of turbine	None
Can et al. (2013)	2 blade helical rotor vs. S-blade (Savonius)	Savonius rotor produces neg. torque coefficient in 2 ranges of operation, while helical does not	
Bachu, Gupta, and Misra (2013)	Helical rotor with 45° twist angle	Significant power increase at rotor angle 90° respect to incoming air velocity	Fig. 5 Sweep surface at centre X=0, Y=1, Z=0
Saha and Rajkumar (2006)	Varied twist angle	Larger twist angle recommended for lower wind velocities	
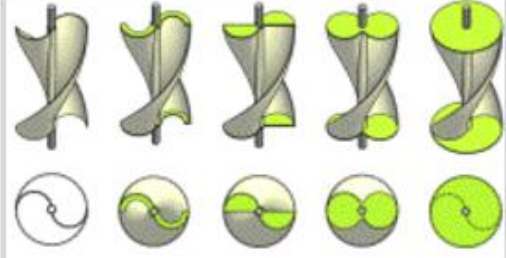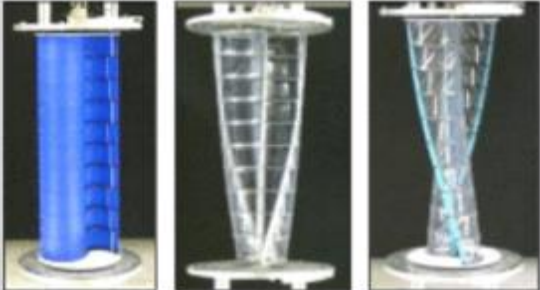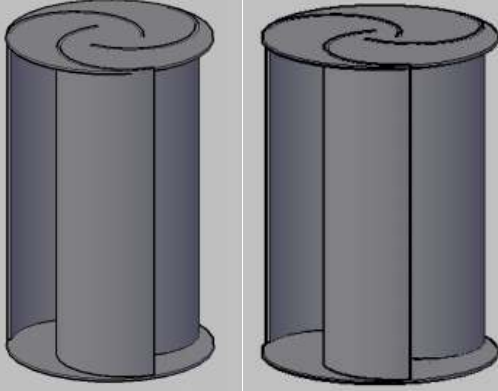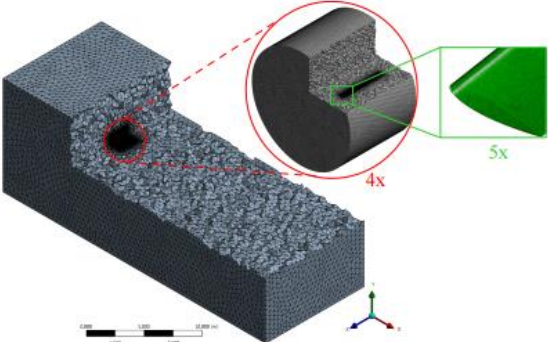
Jeon et al.	End plate size and geometry on 180° twist helical VAWTs	Circular end plates top and bottom increased power coefficient by 36%	
Ricci et al. (2016)	Different configurations for Savonius turbines	Maximum C_p with 105° helical twist, end plates, and central gap	
Morshed, Rahman, and Ahmed (2013)	2D numerical simulation of different overlap ratios for 3 blade Savonius	Highest torque coefficient achieved with 0.12 overlap ratio	
Alaimo et al. (2015)	Development of 3D simulation for helical VAWTs	Tetrahedral elements used to characterize the mesh, second order interpolation for face pressure	
Sagol, Reggio, and Ilinca (2012)	Turbulence models for VAWT simulation	Realizable k-epsilon is recommended to account for flow rotation and strain	None

Table 2.1. Summary of VAWT research (Salyers 2016).

In his work (Salyers 2016), the goal of the study was to compare performance of straight and helical shape turbines. The authors used two-dimensional and three-dimensional approaches to solve the Reynolds Averaged Navier-Stokes (RANS) equations. The research efforts showed that:

- Modifying standard bucket type savonius turbine designs a decreased range of negative torque values can be attained, while increasing the power coefficient.
- Helical rotors with a 90 degree helical twist having 2-4 blades have positive torque values throughout the entire range of motion.
- 3-bladed helical rotors possess the best self-starting capabilities.

2.3 Darrieus Turbines

Darrieus rotors have a higher coefficient of performance and starting torque than a Savonius turbine and work very good in roof installations for energy harvesting. They do tend to have more mechanical stresses than Savonius rotors, but are lower maintenance and less noisy than HAWTs. Illustrated in Figure 2.3 are the different designs of the Darrieus turbine that have been proposed. These designs have begun to take on exotic shapes and are now being explored for their power producing capabilities. Displayed in Figure 2.3 is, (a) Full Darrieus (or eggbeater), (b) "H", (c) the "V" (or "Y" or "sunflower"), (d) "Δ", (e) "Diamond" and (f) "Giromill".
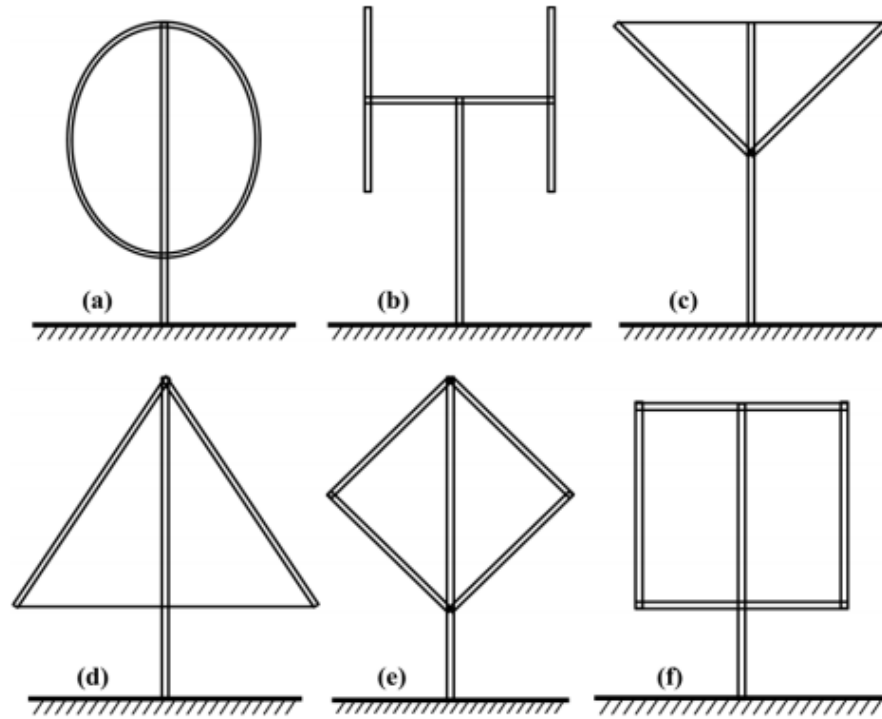
Figure 2.3. Basic Darrieus VAWT Configurations (Sun, et al. 2016).

Numerous researchers worldwide are attempting to identify effects of the key design parameters of the Darrieus rotor, such as the number of blades, blade solidity, and airfoil type on its energy characteristics by means of experimental and numerical techniques (Sun, et al. 2016).

2.4 Rotor Solidity

Solidity is usually defined as the percentage of the circumference of the rotor which contains material rather than air. High-solidity machines carry a lot of material and have coarse blade angles (Kumar and Baredar 2014). Depicted in Figure 2.4 is the visual difference of a high solidity rotor vs. low solidity rotor. From the image it is evident that rotor solidity can have a dramatic impact of turbine performance. Blade/rotor solidity is defined as,

$$\sigma = \frac{N_b C}{2\pi R} \quad (1)$$

where, N is blade number, C is blade chord (m), R is wind turbine radius (m).
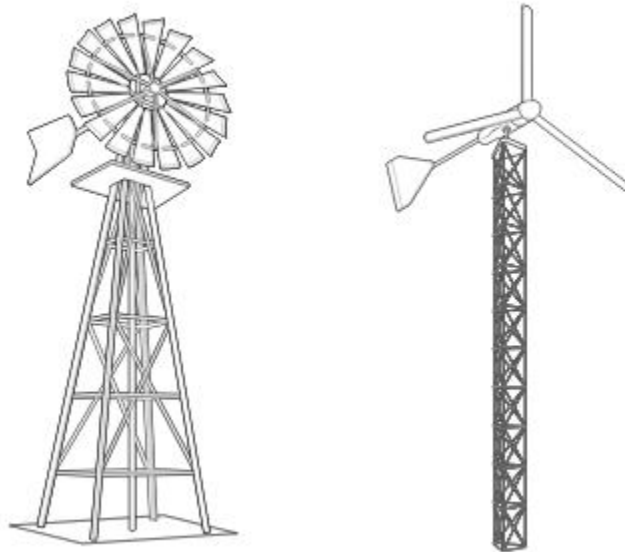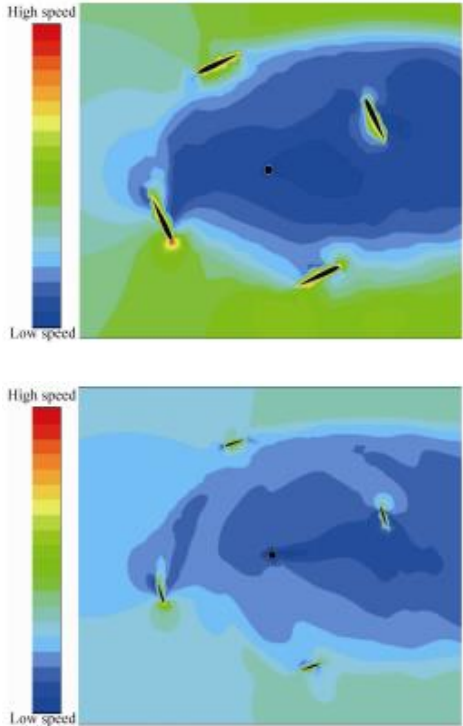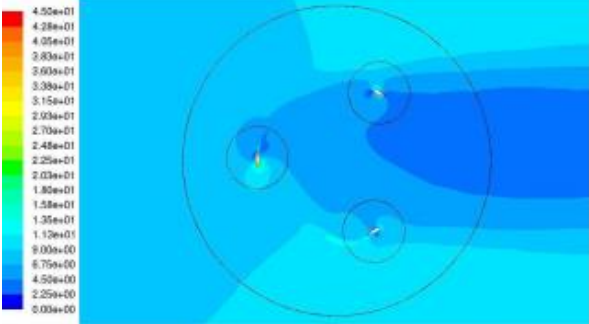
Figure 2.4. High Solidity vs. Low Solidity difference (Vernier Software & Technology n.d.).

Notice from *(1)* that solidity is affected by a number of factors having to do with turbine overall performance. Therefore, solidity is one of the vital keys to designing a viable wind turbine rotor. A series of experimental simulations were conducted by (Q. Li, et al. 2016) to illustrate the improved understandings of the aerodynamics of straight-bladed VAWT performance through wind tunnel experiments, they found that the power coefficients decrease with the increase of the solidity. However, the torque coefficients increase with the increase of solidity.

The results of the work done by (Li and Li 2010), where, a series of numerical simulations were conducted to investigate the influence of solidity on a Darrieus-type straight-bladed vertical axis wind turbine (SB-VAWT), concludes the results of (Q. Li, et al. 2016) by stating that VAWTs

with a larger solidity can achieve higher power coefficients at a lower tip speed ratio, however, a large enough solidity will subsequently decrease the power coefficient. Summarized in Table 2.2 are the results effect of solidity in various research efforts.

Researcher(s)	Studied	Findings	Figure
Li and Li (2010)	The influence of solidity on a Darrieus-type SB-VAWT	Larger solidity achieves maximum power at lower tip speed ratio. However, too large solidity will decrease the power coefficient.	
Castelli, Betta and Benini (2012)	Analyses were performed in order to understand the effect of blade number on the behavior of a SB-VAWT.	More blades achieved larger C_p value at lower angular velocity but at lowered efficiency	
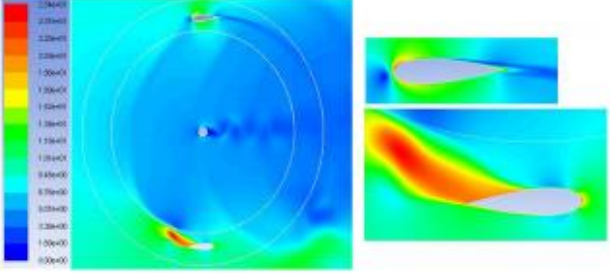
Abu-El-Yazied, et al. (2015)	Simulated power performance of a two, three, four and six-bladed SB-VAWT	Two-bladed rotor configuration shows the best power performance and the obtained peak of power coefficient decreased with the increase in rotor solidity	

Table 2.2. Summary of solidity research efforts.

2.5 Self-starting Capabilities

The Tip Speed Ratio (TSR) is used by wind turbine designers to properly match and optimize a blade set to a particular generator.

$$TSR = \frac{Speed\ of\ blade}{Speed\ of\ wind} \qquad (2)$$

The TSR is important because for any given generator, if the turbine rotor rotates too slowly, most of the wind will pass by, not interacting with the blades. On-the-other-hand if the blades rotate to fast each blade is always moving through the turbulence caused by the previous blade.

TSR's are employed when designing wind turbines so that the maximum amount of energy can be extracted from the wind using a particular generator (Windy 2010).

(Dominy, et al. 2007), states that a machine is deemed to have started if it has accelerated from rest to a condition where the blades operate at a steady speed that exceeds the wind speed (i.e. the tip speed ratio, TSR >1). The criteria of TSR greater than one is added since the blades of the Darrieus are airfoil shaped and are therefore lift-based, unlike, Savonius turbines whose tip speed can't exceed the speed of the wind because they are drag based.

2.6 Structural Characteristics of Darrieus VAWTs

According to a report done by (Sutherland, Berg and Ashwill 2012) for SANDIA National Laboratories, VAWT designs converged on the 2-bladed configuration because, as with 2-bladed HAWTs, this configuration reduced the capital cost of the turbine with only a relatively small reduction in production relative to a 3-bladed turbine. However, the 2-bladed configuration creates some very challenging design problems, as a direct result of the symmetry of the rotor. For 2-bladed VAWTs, the resultant symmetric loadings are important drivers for the in-plane and out-of-plane vibrational modes of the rotor, the two lowest natural frequencies of the rotor (Sutherland, Berg and Ashwill 2012).

The "Y" configuration, also called the "V" configuration, is an interesting design concept for off-shore platforms. As opposed to the "H" design, the blade-to-tower joints are moved inboard to the base of the tower, thus reducing the aerodynamic losses from these joints. However, many of the designs require struts (cables) to stabilize the ends of the cantilevered blades. With molded composite blades, the struts can probably be -56- eliminated entirely, or at least moved down the blade and/or aerodynamically faired to minimize aerodynamic losses (Sutherland, Berg and Ashwill 2012).

Unlike the HAWT where the blades exert a constant torque about the shaft as they rotate, a VAWT rotates perpendicular to the flow, causing the blades to produce an oscillation in the torque about the axis of rotation. This is due to the fact that the local angle of attack for each blade is a function of its azimuthal location.

According to, design standard IEC61400-2, put forth by the International Electro-technical Commission, there are three instances where a turbine will experience increased loads, which must be considered in the designing of a wind turbine, these are:

- Vibrational, Inertial and gravitational loads

- Aerodynamic loads

- Operational loads

Since the criteria for the success of this research is that a maximum power coefficient (C_p) must be attained within the range of a conventional straight-bladed H-type Darrieus rotor, we must establish from existing work what this criteria is. The comparison of various achieve C_p values is listed in Table 2.3.

Author(s)	Scope of Research	Achieved Power Coefficient
(Kjellin, et al. 2011)	Experimental study observing the performance of a 12kW H-rotor VAWT	0.29
(Parra, et al. 2014)	This study was a review of H-type VAWTS, where flow patterns and the effect of solidity were studied.	0.303 at a rotor solidity of 1.0 0.216 at a rotor solidity of 0.5 0.104 at a rotor solidity of 0.3
(Rezaeiha, Kalkman and Blocken 2017)	In the existing literature the effect of pitch angle on VAWT performance is investigated	0.35 CFD and 0.31 experimental
(Q. Li, et al. 2017)	The work evaluated the effects of the rotor aspect ratio (AR) and solidity (different chord lengths and blade spans) on the performance of straight-bladed VAWTs.	0.183 at a rotor AR of 0.4 0.223 at a rotor AR of 0.6 0.247 at a rotor AR of 0.9 0.273 at a rotor AR of 0.1.2

(Chougule and Nielsen 2014)	An overview of different pitch control methods are discussed and further a multi body approach is used to design a self-acting pitch control linkage mechanism.	0.33 results without pitch control 0.4 results with pitch control

Table 2.3. Power Coefficients of straight-bladed VAWTs in various research works.

The data depicted by Table 2.3 suggests that a power coefficient value within the range of 0.18 to 0.40 would be satisfactory for this experiment to be called successful.

2.7 Inertial, Vibrational and Gravitational Loads

According to the IEC61400-2, inertial and gravitational loads are loads which result from static or dynamic loads, inertia, gyroscopic vibration, rotation, gravity and seismic activity that may affect the turbine or its support. The manual also states that special attention should be given to natural frequencies of the blades and structural components of the turbine.

2.8 Aerodynamic Loads

Aerodynamic loading is caused by the interaction of the air flow with the turbines stationary or moving parts. This loading can be static or dynamic.

2.9 Operational Loads

Operational loads according to the (IEC TC 88 2006) manual are loads which result from the operation and control of the wind turbine system, such as yawing, pitching, braking, furling, and grid connection.

2.10 Other Loads

Other loads on the turbine may arise from transportation of the system to its designated commissioning location, wake loads which result as each blade passes through the wake of the previous blade, ice loads, maintenance and repair loads.

2.11 Load Cases

The IEC61400-2 guideline also lists load cases for which to design, in the case of a SWT. Table 2.4 represents the various load cases.

Design Situation		Load Case	Wind Flow	Remarks
Power production	**A**	Normal operation		
	B	yawing	$V_{hub} = V_{design}$	
	C	yaw error	$V_{hub} = V_{design}$	
	D	Maximum thrust	$V_{hub} = 2,5V_{ave}$	Rotor spinning but could be furling or fluttering
Power production plus occurrence of fault	**E**	Maximum rotational speed		
	F	Short at load connection	$V_{hub} = V_{design}$	Maximum short-circuit generator torque
Shutdown	**G**	Shutdown (braking)	$V_{hub} = V_{design}$	
Parked (idling or standstill)	**H**	Parked wind loading	$V_{hub} = V_{e50}$	
Parked and fault conditions	**I**	Parked wind loading, maximum exposure	$V_{hub} = V_{ref}$	Turbine is loaded with most unfavorable exposure
Transport, assembly, maintenance and repair	**J**	To be stated by manufacturer		

Table 2.4. Design load cases for the simplified load calculation method, (IEC61400-2).

2.12 VAWT Structural Analysis

(Staino and Basu 2015), states that there is a challenge in understanding the dynamic properties of wind turbines via analytical, numerical, and experimental means.

Many of the vibration and noise related problems contribute to resonance. The resonant vibration is mostly caused by interactions between the elastic and inertial properties of the materials of the structure since small forces can cause important deformations, and possibly, serious damages (Sellami, et al. 2016).

2.13 Static Structural

The structural design of VAWT turbines have come a long way. Borrowing techniques from established practices exercised by horizontal axis wind turbines, research conducted by (Roscher 2014), found that by placing thicker high drag NACA 4 digit airfoils at the roots of a φ-shaped vertical turbine led to a reduction in angle of attack (and thus improved performance), and lent itself to a more structurally stable blade. (Roscher 2014), also performed an aero-elastic analysis which showed that the displacements of the blade increased with the tip speed ratio. Conclusions of this study asserted that maximum power losses of 5% were observed due to the flexibility of the blade.

(Hussen, et al. 2015), performed a study in which they compared the structural results of 3 types of VAWTs (two Helical models and a straight bladed design), to variable wind loads. In this simulation based analysis the stress values are significantly increased for rotors with twisted geometry compared to straight-bladed models, however in this work the values did not exceed the elastic limit of the materials being tested.

2.14 Fatigue Stress

When doing a fatigue analysis there are several inherent issues surrounding this type of loading. Materials tend to fail much sooner than their structural limit parameters when experiencing fatigue loading. This is the case because cyclical loading affects a material in a much different way than static loading does. The main obstacle with fatigue loading is that it causes cracks within a material whether on a micro or a macro scale. These cracks then develop and propagate through the material to eventually cause failure of the material (Marín, et al. 2009). It is for this reason that the analysis of fatigue stress on a wind turbine blade is important. Wind turbine blades whether HAWTs or VAWTs experience, cyclical loads from rotation, gravity and vibration just to highlight a few. Analyzing the threats posed by these types of loads will lead to more reliable wind turbine designs as they grow in size and become more varied in shape and application.
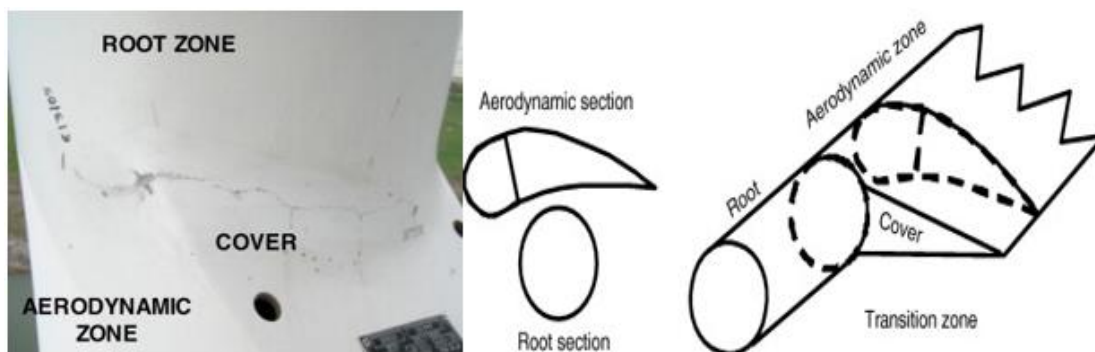
Figure 2.5. Effect of Fatigue on a wind turbine blade (Marín, et al. 2009).

(Tawade, Todkar and Hade 2014), states that in HAWTs fatigue is mostly a function of azimuth angle (ψ), however, in VAWTs it is mostly a function of wind speed (Veers 1981). A study conducted by (Barnes, Morozov and Shankar 2015), where The objective of the study was to quantitatively compare high and low wind speed blade structures the results indicated that, issues such as fatigue and fluid–structure interaction are more significant in LWS than HWS blades. Figure 2.5 depicts a view of the damage that is caused by cyclical fatigue loading.

There was a project led by the Sadia National Laboratories and FloWind Corporation, where they developed and installed many VAWTs in California, before widespread fatigue failure in the turbine blades drove the company out of business years later. This was due to materials and manufacturing methods that were not well-suited for the fatigue loads VAWT turbines experienced, which were not well understood at the time. This drove a perception in the industry that VAWTs were prone to fatigue (Veers 1981), (Brown 2016). The maximum stress is obtained when the blade is rotating at cutout wind speed while the minimum stress is obtained when the turbine is rotating at the cut-in wind speed (Tawade, Todkar and Hade 2014).

2.15 Modal Stress

The magnitudes of vibratory stresses in the blades can be reduced by analysis of the resonant modes and frequencies of the operating turbine and judicious design to keep the inherent periodic loads from exciting any resonance (Veers 1981). The main reason to perform a modal analysis is to assess the different mode shapes for likely vibrational responses to loading.

2.16 V-shaped Design

The V-shape Darrieus type rotor is just one of the many rotor developments in recent years as was stated in section 2.3 of this work. The rise of alternative designs is owed to new application potential of VAWT turbines and have led to research efforts seeking to capitalize on configurations that possess the best harnessing potential. Much like any other wind turbine design, the major features of this design that needs to be scrutinized heavily is the structural and aerodynamic characteristics.

2.16.1 V-shaped Structural Study

In order for VAWTs to achieve equivalent potentials as those proven to be characteristic of HAWTs, they end up being huge and often with longer and more flexible blades than HAWTs. (Owens and Griffith 2015). Dynamic aero elastic instability or flutter can be a concern for lift-generating structures under aerodynamic loads. Coupling of aerodynamic forcing with a structure's natural modes can lead to large amplitude diverging motion. Recent studies have shown that blade flutter is a potential issue in very large HAWT wind turbine blades and may be a concern for very flexible multi-megawatt VAWT structures under large aerodynamic loads as well (Owens and Griffith 2015). (Owens and Griffith 2015), carried out a study where they scrutinized preliminary VAWT configurations for the purpose of identifying aero-elastic instabilities. From this study they derived that, overall, the multi-MW VAWT designs considered in this paper had sufficient aero-elastic stability margins with aero-elastic instabilities occurring outside of operational rotor speeds (Owens and Griffith 2015). Therefore, it was noted by the study that other drivers may present to be of greater importance than aero-elastic stability.

(Wang, et al. 2016), conducted a study where their efforts focused around developing a structural optimization model applied to a V-shaped airfoil shaped blade. They worked with variables such as blade mass buckling load, deformation and stress. A genetic algorithm found the optimal blade statistics from mass of the blade with multi-criteria constraint conditions, number of unidirectional plies, location of the spar cap and material thicknesses were taken as the design variables in the algorithm. The study showed good agreement with studies conducted by WindPACT 1.5 MW modal analysis study showing a percentage difference of about 2.63%. They assert that their methods are transferable to other structural optimization scenarios concerning wind turbine composite blades.

2.16.2 V-shaped Aerodynamic Study

In efforts carried out by (Shires 2013), his study describes the development of an aerodynamic performance model specifically for a novel V-shaped VAWT rotor with multiple aerodynamic surfaces, based on the Double-Multiple Streamtube method. This work studied the effects of tip, tower and junction loses on the comparison of several different turbines in existence of various traditional Darrieus VAWT configurations. (Shires 2013), found that, the predicted power for a prototype of the V-shaped VAWT with multiple blades is in reasonable agreement with measured data. Whilst more detailed measurements are necessary to fully validate the model, by demonstrating that power curves for both H- (with relatively large tip effects) and Φ- (with relatively small tip effects) shaped rotors can be predicted with reasonable accuracy, this evaluation study provides confidence that the tool is also appropriate for assessing the performance of V-VAWT concepts with potentially large tip effects (and considering that junction effects are relatively small).

CHAPTER 3

METHODOLOGY

3.1 Introduction

As outlined in (Manwell, McGowan and Rogers 2009) there are numerous methods available to design an adequate wind turbine. (Manwell, McGowan and Rogers 2009), outlines twelve steps from concept to production of a working wind turbine. These steps are outlined as follows:

1. Determine application.

2. Review previous experience.

3. Select topology.

4. Estimate preliminary loads.

5. Develop tentative design.

6. Predict performance.

7. Evaluate design.

8. Estimate costs and cost of energy.

9. Refine design.

10. Build prototype.

11. Test prototype.

12. Design production machine.

For this project these established methods of designing and analyzing an optimal VAWT rotor blade will be refined and pursued.

SolidWorks software will be utilized to define the CAD geometry after which ANSYS will be applied as a Finite Element Analysis (FEA) tool, in order to determine the structural and

aerodynamic characteristics of the proposed VAWT design. An open-type subsonic wind tunnel is used for the experimental portion of this thesis. Where 3D printed blades are analyzed for RPM, static torque and wind dynamics around the turbine. These efforts are detailed in this section.

3.2 Aerodynamic Blade Design

Based on the steps lain out previously, (Perry 2015) refined these steps for research proposes and proposes the steps laid out in Figure 3.1.
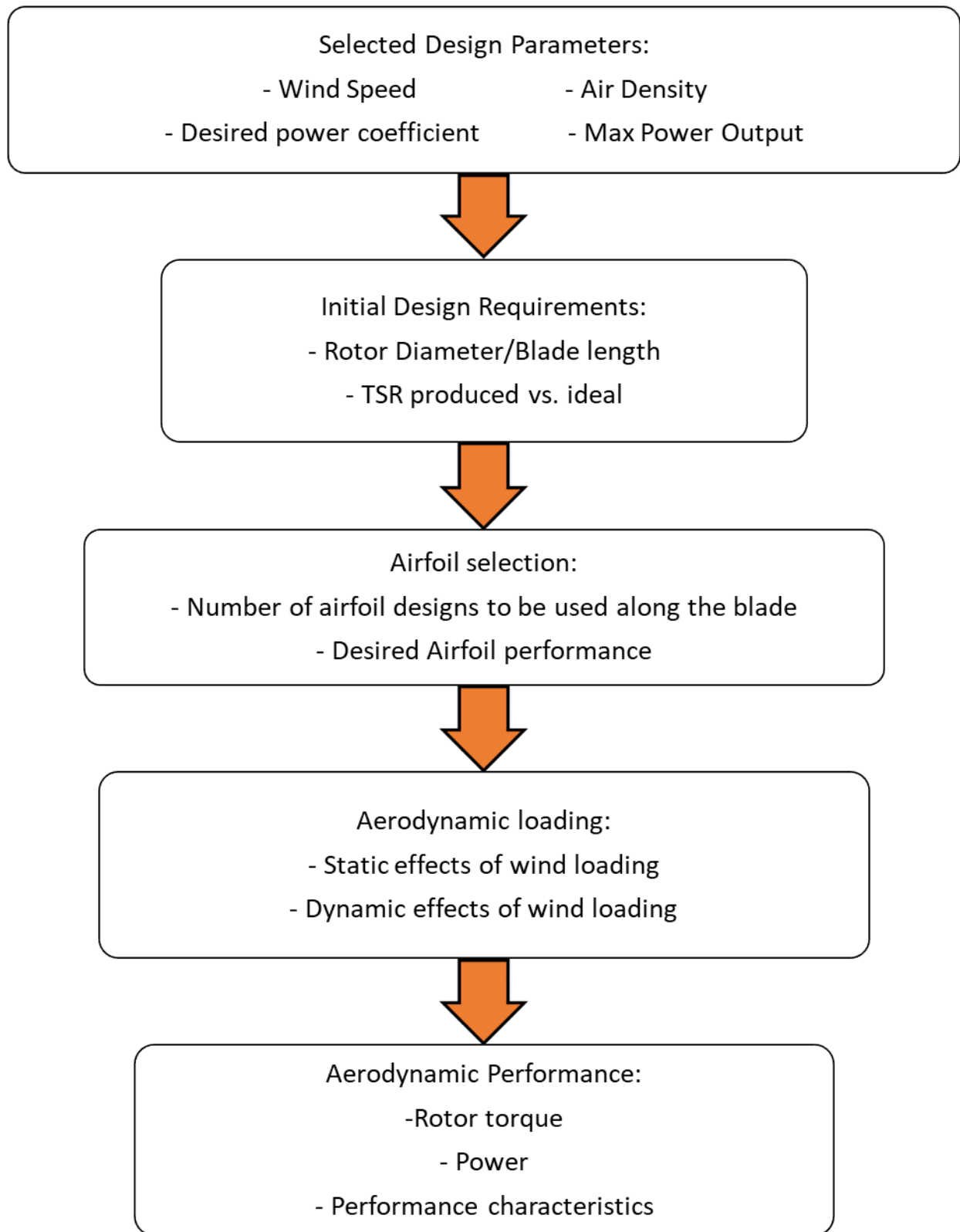
Figure 3.1. Optimized blade aerodynamic performance and loading calculation (Perry 2015).

The turbines area was first determined through the use of the extracted power equation defined by:

$$P_{extract} = \frac{1}{2}\rho A_S V^3 C_P, \qquad (3)$$

This equation was rearranged and solved for rotor area with the information for the initial VAWT rotor blade design parameters in Table 3.1.

Number of Blades (B)	5
Wind Speed, Design (m/s)	8
Power, Design (Watts)	5.5
Air Density, Sea Level (kg/m^3)	1.225
Swept Rotor Area (m^2)	~0.0725
Power Coefficient, Design (-)	0.25

Table 3.1. Overview of the starting VAWT rotor blade design parameters.

3.3 Model Design and Fabrication

SolidWorks is used to design 3 different rotor designs. These designs follow the basic Schematic laid out in Figure 3.2. This layout will be used for the structural analysis of the blade and by extension the rotor. The five blades of this turbine are designed to be identical and so it is assumed that the moments, forces, modal shapes and fatigue assessed in one blade will be identical in all blades at some time during the turbines operation. As a result only one will be modeled in this study to analyze and estimate the effects of the wind on the turbines structure.
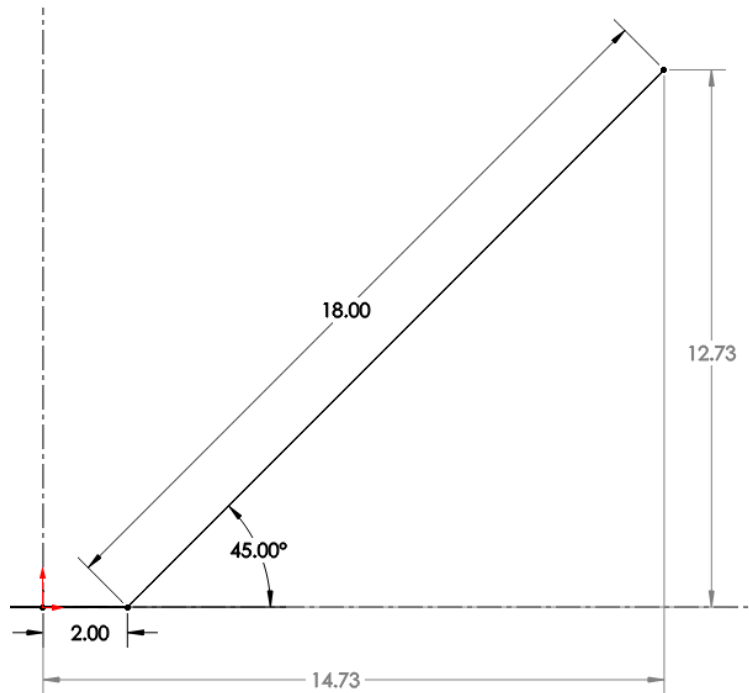
Figure 3.2. Schematic of intended test blade.

As can be seen from the Figure 3.2, there are two main parts to the blade anatomy, i.e. the shoulder and the arm. The blade arm is approximately 18.00 inches from the connection at the shoulder to the blade tip. The shoulder length is 2.00 inches and the radius and height are 14.73 inches and 12.73 inches respectively. For the purpose of the structural study, all models will be mounted at an inclination angle of 45 degrees angle from horizontal plane.

Figure 3.3. Blade designs 1, 2 and 3 respectively.

The three blade designs that are proposed are illustrated in Figure 3.3. The description of each blade is described in Table 3.2. Notice from the table the three different blade root connection configurations. This was done so that the blade root configuration that was most structurally reliable and easiest to fabricate can be implemented. The central spar type configuration was considered in the event foam was chosen as the design material it would be easy to affix it to the rotor. It is designed so the rotor will have an aluminum (or wood) spar that will run through center of the blade profile its entire length and then fixed in place with a wooden spar-cap. The spar-cap and aluminum spar not under study in this work.

Design	Section	Chord (in)	Profile	Blade Root connection type
1	Shoulder	2.25	NACA0015	Dove-tail
	Arm	1.75	NACA0015	
2	Tip (Arm)	1.00	NACA2414	Male-female socket
	Root	2.50	NACA0040	
3	Tip (Arm)	1.50	NACA2414	Spine insert
	Root			

Table 3.2. Design specifics of blade designs.

Each airfoil is applied to blades considering time to model each blade adequately in SolidWorks, manufacturability, complexity and aerodynamic qualities such as lift and drag.

Based on the lift and drag characteristics found from (Xfoil n.d.), the NACA 2414 was chosen to be used for the blade construction of blades 2 and 3. NACA 0040, was applied because it offers good structural characteristics having a thicker profile than other profiles mentioned here. The NACA 0015 airfoils were employed to blade design 1 because it routine to use this design as a starting point for blade profile geometry and it offers the advantage of being easy to work with since blade 1's design was more complex than the other 2 cases.

3.4. Model Development

Moving down the list from Figure 3.1, we move from selecting the airfoil shape that will be applied to producing a working CAD model that will later be moved to the additive manufacturing stage. Blade designs 1 and 2 are much simpler. Blade design 2 is a typical HAWT blade, while design 3 is more akin to a typical Darrieus turbine blade whose geometry is constant throughout the blade profile. Each blade when mounted will fit the rotor anatomy described in Figure 3.2.

3.4.1. Additive Manufacturing and ABS Plastic

Additive manufacturing is the official industry standard term for all applications of the technology. It is defined as the process of joining materials to make objects from 3D model data, usually layer upon layer, as opposed to subtractive manufacturing methodologies (F2792 −12a 2013). One of the main mediums of this type of manufacturing is ABS thermoplastic. Figure 3.4 depicts the 3D printing process of blade design 1.

Figure 3.4. 3D printing of ABS Blade.

The models proposed are exported to an FDM 3D printer and printed in ABS plastic. ABS plastic is made by variation of the ratio of the three monomers Acrylonitrile, Butadiene and Styrene. Its uses are varied in industry due to its ability to be mixed with various other compounds and polymers to create a hybrid polymer that can have characteristics such as heat resistance, increased stiffness (through added fiber reinforcement), high and medium impact, etc. Because of it high ability to be molded (lending to ease of manufacture), quality surface finish and its ability to flex before rupture, when stress is applied, this plastic is ideal modelling the proposed turbine blades. *Table 2.1*Table 3.3 sums up the characteristics of ABS plastic that are applied in this work.

Criteria	ABS Plastic
Density (kg/m^3)	1030
Young's Modulus (GPa)	2.62
Poisons Ratio	0.34
Ultimate tensile strength (MPa)	71.5

Table 3.3. Mechanical Properties of ABS plastic. (Caliskan, et al. 2016) and (Bourell 2017).

The 3D printer deposits the ABS plastic layer by layer along with a support material to form the blades structure. The plastic is deposited onto the build surface pad, and adheres to it; this allows models to stay in place as the printer head is moving through its path. After the printing is done, the parts can be lifted off using a flat edge, and then is placed in a solution of water and lye to dissolve any remaining support material.

3.5. Blade Loading

(Ju and Sun 2017), states that, a rotor/blade system undergoes both gross rotational motion and small elastic body motions. In general, the blade elastic body motion includes the flapwise and edgewise bending deflection, as well as the axial and torsional deformation. Of all the deformations, flapwise deflection receives the most attention not only because of its relatively large magnitude compared to the edgewise deflection but also because of its direct influence on aerodynamic loading.

In the configuration we are applying, this wind turbine blade is a cantilever, with the root constrained and the tip free. The gravitational force in the case of the proposed design is in the flapwise direction with wind flow acting in the edgewise direction. Unlike conventional HAWT turbines where gravitational forces affect the blades in the edgewise fashion and the direction of loading is reversed throughout the rotors travel, many VAWT blades tend not to have this issue as

the blades are oriented so that their gravitational forces on the blade are negligible (Barnes, Morozov and Shankar 2015). Figure 3.5 is a depiction of flapwise loading versus edgewise.
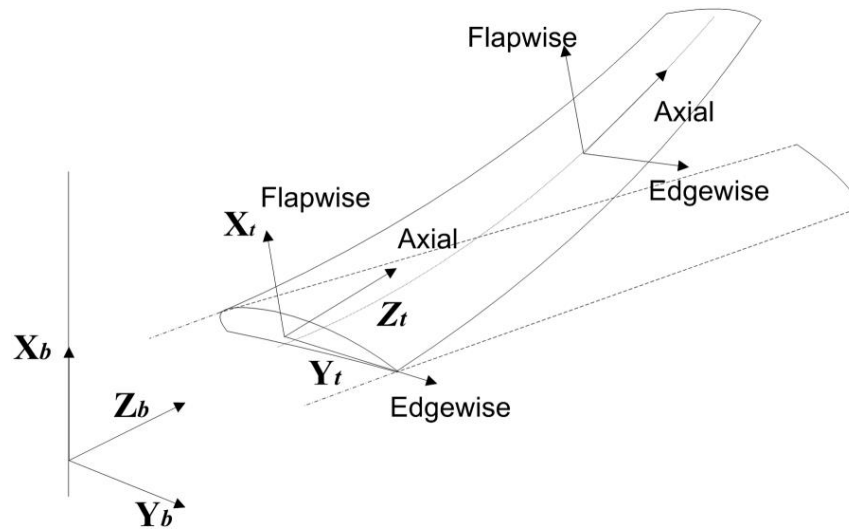
Figure 3.5. Flapwise vs. Edgewisse loading (Barnes, Morozov and Shankar 2015).

3.6. Experimental Model and Equipment

The Georgia Southern wind energy laboratory is equipped with a subsonic open-type wind tunnel for experimental testing. The existing wind tunnel and test section are depicted in Figure 3.6. The wind tunnel inlet can be seen in the far right of the photo, followed by a honeycomb section for laminar flow. The fan is controlled by a Huanyang variable frequency drive. Another honeycomb section immediately follows the fan. Next is a diverging-converging section with a 9 to 1 area ratio to the 2 ft. by 2 ft. wind tunnel outlet. The VAWT test section frame is also showed at the wind tunnel outlet (Salyers 2016).

Figure 3.6. Wind tunnel configuration.

3.7. Wind Speed

Free stream velocity through the test section is easily controlled with the variable frequency drive (VFD) operator interface depicted in Figure 3.7. Consistent and maintainable RPMs of the motor depend on the frequency, measured and displayed in Hertz, transmitted from the VFD. The internal fan produces wind speeds of 0 to 13 m/s through the outlet (Salyers 2016).

Figure 3.7. Huanyang variable frequency drive operator interface.

A handheld anemometer is used to track wind speeds at the beginning of each run. Similar to the methods applied by (Salyers 2016) the instrument was held about 4-6 inches in front of the model.

Figure 3.8. Handheld anemometers used for wind speed measurement.

There were 5 separate readings of wind velocity taken from each anemometer (10 readings total) and averaged at each wind velocity. To ensure consistency and accuracy the measurement is taken over a period of 5 seconds. The anemometers being used in this experiment are pictured in Figure 3.8. The La Crosse Technology anemometer has a range of 0.2 to 30 m/s and is accurate to 0.1 m/s, while the CFM Master II is of higher precision, has a measurement range of 0.4 to 35 m/s, and accuracy of +/-3%.

3.8. Test Hub Turbine

In this study a reference turbine is utilized for the experimental portion of the study in order to have a base design from which to begin designing our rotors. The reference turbine is the *ALEKO® WGV15 Vertical Wind Turbine Generator 15W - 12V*, which is a standard 5-bladed H-type Darrieus VAWT. The turbine can be viewed in Figure 3.9.

Figure 3.9. ALEKO WGV15, Reference turbine (Newegg.com n.d.).

Figure 3.10 details the technical specification as provided by the manufacturer. It should be noted that this turbine is slightly larger than our proposed design. An area of 0.073 m^2 was calculated for the test model while this turbine is about 0.10 m^2.

Technical specification	
Performance	
Rated power	10W @10m/s
Peak power	15W
Start-up wind speed	2m/s
Working wind speed	3-20m/s
Survival wind speed	35m/s
Noise	≤40dB
Rotor	
Rotor diameter	310mm
Swept area	$0.1m^2$
Blade	5pcs alumimium alloy
Blade length	300mm
Shell material	Erosion resistant aluminum
Rated RPM	400
Weight	2.3KG
Others	
Generator type	3-phase AC PM, gearless
Speed regulation & protection	overvoltage charge controlling
Rated voltage	DC 12V
Suggested battery capacity	1pcs 7AH/12VDC
Tower type	3-6m guyed cable tower
Working temperature	-30-50℃

Figure 3.10. ALEKO WGV15 Technical Specifications (Newegg.com n.d.).

The turbine out of the box operates very quietly. The technical data from the manufacturer indicates that the turbine operates at about 40dB, which, to put this in perspective is about the same volume level as a library. The turbine operates very well over a wide range of wind velocities, and self-starts at about 6m/s.

There was quite a large portion of this project that was designed around the ALEKO turbine being used as a reference. The rotor hub design applied is illustrated in Figure 3.11 and Figure 3.12. The hub design was developed and tested going into the aerodynamic testing phase to ensure it had good structural integrity, however, since the blades are more consequential to turbine failures, they were the focus of this study.
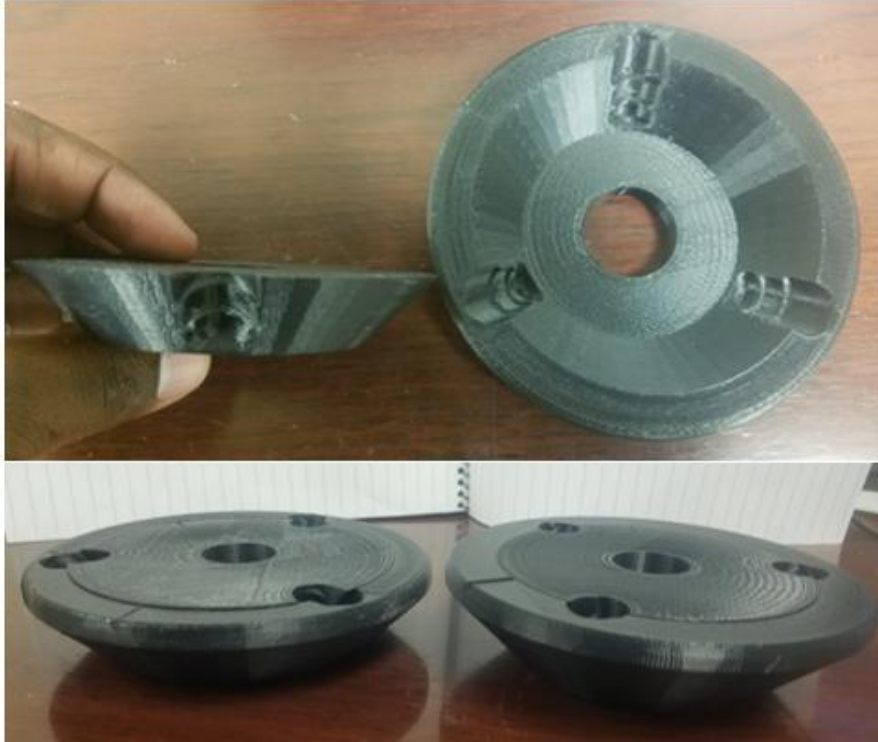
Figure 3.11. Rotor Hub design showing inner locking cap plate and outer hub (upper). The 3 bladed 45 degree hub and the 3 bladed 60 degree hub side by side (lower).

Figure 3.12. ALEKO WGV15 Assembly (left). Test hub design installed on ALEKO hub (right).

The hub was mounted to the ALEKO generator hub and held in place by a 1 inch washer and ½" nut that came with the ALEKO assembly. This design allowed for the blades to be adjusted for pitch angle as well as utilize the same hub for multiple rotor configurations. In all, four hub models were created, but only 3 were applied to the efforts of this thesis.

The hub design applied in this work was developed in order to:

1. Facilitate multiple blade designs to be tested using the same hub.

2. Accommodate the variable of inclination angle (Separate hub designs had to be created for 60 and 45 degree angle of inclination.)

3. For there to be more uniformity throughout the project.

4. Create a hub design that would allow for interchangeability.

3.9. RPM Measurement

For the purposes of RPM measurement the turbine was affixed to the ALLEKO Hub seen in Figure 3.13. The RPM of each wind turbine rotor is measured 5 time at each wind speed and then averaged to give the final values reported in this work.
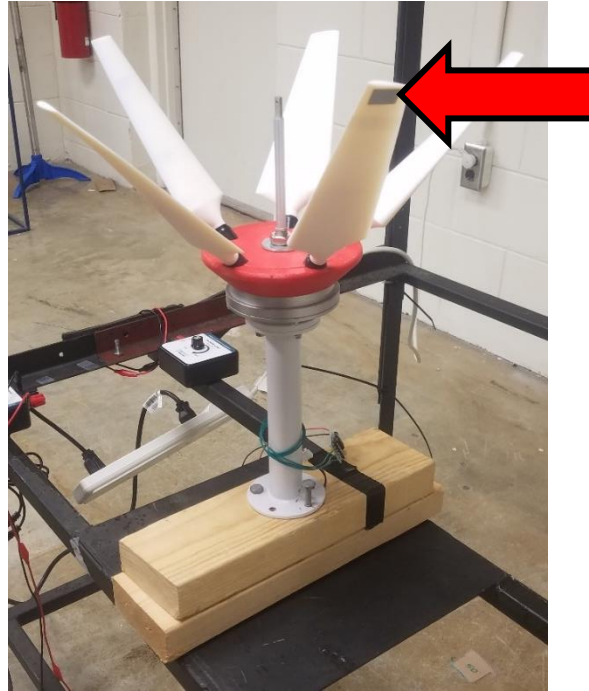
Figure 3.13. RPM measurement set-up denoting the placement of reflective tape.

A laser tachometer is used to measure RPM of the models under varying wind conditions, as illustrated in Figure 3.14.

Figure 3.14. Laser tachometer for RPM measurement.

A small piece of reflective tape, indicated by the red arrow in Figure 3.13, is applied to the top of one blade to reflect the infrared light. A detector on the tachometer receives the reflected

light and detects changes in frequency. The frequency change over time gives the rotational speed of the VAWT models (Salyers 2016).

The Omega HHT12 is able to measure RPM accurately from angles up to 30 degrees off perpendicular and up to 36 inches from its target. It measures RPMs in the range of 5 to 99,999 RPMs and an accuracy of +/- .01% of reading.

3.10. Static Torque Measurement

A reactional torque meter is used to gage the torque as it relates to the increase of wind speed. For each wind speed, torque is recorded every 20 degrees of turbine rotation. The torque meter is calibrated using a dial torque wrench. Depicted in Figure 3.15, is the Lutron TQ-8800. It can monitor torque in 3 different units (Kg_f-cm, Lb_f-in and N-cm), and has a maximum of 147.1 N-cm. The accuracy of the device is +/-1.5%. Each segment of the plate exhibited in the Figure 0.18 represents 10 degrees of rotation.
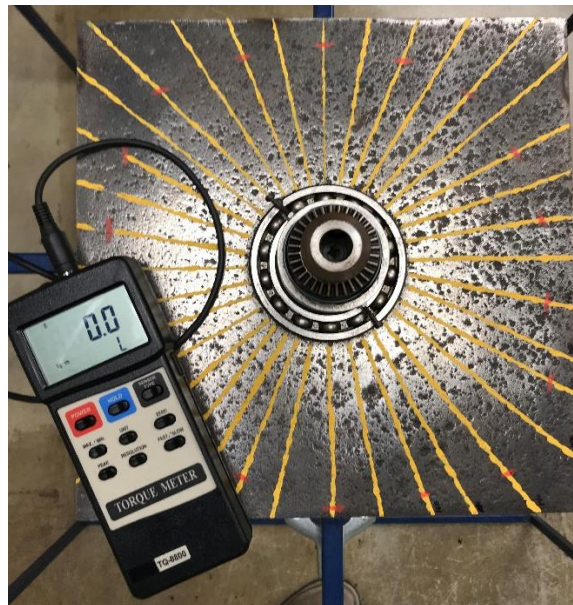
Figure 3.15. Lutron TQ-8800 torque meter configuration.

The experimental setup for torque measurement had to be specifically designed for this project. The torque meter in Figure 3.15, has a chuck clamp and will only fit an $\frac{11}{16}$ (0.5625) inch shaft, therefore a mechanism has to be designed to fit this chuck that will be rigid enough to withstand the wind loads as well as the weight of each turbine model configuration while holding the assemblies in place so that an accurate torque reading can be acquired.

Figure 3.16. Torque measurement lock-shaft.

Pictured in Figure 3.16, is a shaft lock-up designed in SolidWorks and 3D printed using ABS plastic, to accommodate the purposes specified. Observe from the figure the smaller pieces which serve as the portion that locks the shaft in place, these pieces also had to be designed separately so as to accommodate both rotor setups, since, the 60 degree rotor hub was about 3/8 (0.375) inches taller than the 45 degree rotor hub. All pieces included in this assembly have a center-bore hole designed to accommodate a ¼" bolt that will keep the assembly together and lock in place during testing. The top view of these printed parts shows the key slots where the lock

portion of the mechanism fits into the shaft to hold the rotor in place. The assembled rotor with lock-shaft affixed to the torque meter is exhibited in Figure 3.17.

Figure 3.17. Torque test assembly, with shaft lock-up.

It is important to note that all blades root sections, rotors hub sections, and torque measurement lock-up techniques were designed using ASME Y14.41-2009 standard for dimensioning and tolerance.

3.11. Numerical Analysis

This section is divided into two parts, the static methodology applied in this project and the aerodynamic methodology applied. The structural section will be further divided, and will discuss the static loading response of the V-shaped wind rotor, then fatigue loading as well as modal analysis will be observed. In the aerodynamic section, both experimental and numerical aerodynamic analysis will be done by assessing static torque reactions, all assessed data will be from this variable. This section will seek to discuss what settings were chosen and why, and also

give some pertinent information about the various parameters and boundary conditions being applied.

In an effort to study the structural and aerodynamic characteristics of the various rotors in this study, numerical simulations are performed using commercial Computational Fluid Dynamics software, ANSYS CFX version 18.2 and 19.1.

3.11.1. Static Structural Analysis

Observing the three load instances lain out in Section 2.3.3, and various wind loading scenarios in Table 3.4, this work will focus on the aerodynamic, vibrational and gravitational loading instances; the load cases that will be assessed are, parked 50 year storm conditions, Static loading due to gravity as well as aerodynamic loads that may occur due to centrifugal force and inertia instances such as critical mode shapes and modal analysis.

The equation given in The International Electro-technical Commission's (IEC), IEC61400-2, sums up the force from impending wind (Aerodynamic force) as follows:

$$F_a = C_f \frac{1}{2}\rho V^2 A_B, \quad (4)$$

where, C_f, is the force coefficient, and can either be from lift or drag; and AB is the component area that is appropriate for the force coefficient. For airfoil shapes, the area shall be the planform area [17]. The design wind pressure, p_z can be represented by the expression:

$$p_z = \frac{1}{2}\rho V^2, \quad (5)$$

and represents the pressure exerted by the wind at any height, z.

The aerodynamic loads due to a parked rotor are depicted for each wind speed in Table 3.6. These pressure loads will be implemented to assess the structural response of the blades.

Wind Speed (m/s)	Pressure Load (Pa)
8 (design wind speed)	39.232
15	137.925
18	198.612
21	270.333
24	353.088
27	446.877
30	551.700
33	667.557
36	794.448

Table 3.4. Wind speeds and corresponding pressure loads.

In Table 3.5 the force result as a function of wind velocity is depicted. These force will be used to analyze the bending moments acting on each blade. The aerodynamic force was calculated for each blade design from *(4)* using lift force data obtained from (Xfoil n.d.).

The International Electro-technical Commission (IEC), utilizes an equation for which they state estimates the wind gust an area may experience overtime based on its average wind speed. This is defined as the 50 year storm wind velocity:

$$V_{e50}(z) = 1.4V_{ref}(z/z_{hub})^{0.11}, \quad (6)$$

where,

V_{ref} is the reference wind speed averaged over 10 min.

Z_{hub} is the hub height.

Parameters (m/s)	Class I	Class II	Class III	Class IV
Average wind speed	10	8.5	7.5	6
50 year return gust speed	70	59.5	52.5	42

Table 3.5. Wind classification definition.

In this work we will assume the expression $(z/z_{hub})^{0.11}$ is be equal to 1.0, since the turbine under study is not mounted at any height. From Table 3.5 we can see where there are averaged wind speeds and the corresponding gust wind velocities. According to (AWS True Power n.d.) In Georgia we encounter average wind speed of 4 to 5.5 m/s annually. This is below any of the listed reference wind speeds, therefore, the scale will be adjusted to make it applicable to our needs. This was done by plugging in values in to equation *(6)* for a class IV wind situation. This results in a wind gust factor of 58.8 m/s. However, as was previously stated we want to apply our design for low wind application, therefore we will take 60% of this calculated value. This gives about 35.28 m/s. Therefore we will round up and take 36 m/s as our maximum extreme wind condition in this work. Rounding up was done to compensate for uncertainty by choosing a maximum gust value slightly higher than what was calculated. Thus a wind range of 15 m/s to 36 m/s was chosen. This range will be used to assess all Static Structural analysis.

WIND SPEED (M/S)	B1 DESIGN (N)	B2 DESIGN (N)	B3 DESIGN (N)
8	114.65	94.12	44.49
15	403.07	330.88	156.42
18	580.43	476.47	225.24
21	790.03	648.53	306.58
24	1031.87	847.06	400.43
27	1305.96	1072.06	506.79
30	1612.30	1323.53	625.67
33	1950.88	1601.47	757.06
36	2321.71	1905.88	900.96

Table 3.6. Wind speed with resulting forces.

The data held in Table 3.6 portrays the forces calculated from equation *(4)*. These forces will be used to assess bending moments. The total force acting on the turbine parts is the sum of aerodynamic force and centrifugal force:

$$F_t = F_a + F_c, \quad (7)$$

where,

$$F_c = \frac{mV^2}{r}, \quad (8)$$

Equation *(8)* will be used to assess the force acting on the rotating turbine. This result will then be used to numerically obtain the reaction of the final test turbine that will be assembled from the blade that is chosen.

When considering the static structural analysis the selected blade geometries, it was considered that due to the design of the blade and the fact that the size of these blades were small, there would not be any sufficient gravitational forces from the blades weight to cause it to fail structurally. The same was assumed of edgewise loading. Therefore the loading on the blade will only be performed in the flapwise direction.

Wind load mapping is done as a preliminary step in CFX just to assess how the wind was interacting with the blade, and also to determine, what, was the most ideal way to represent each loading condition in the ANSYS Mechanical Modeler.
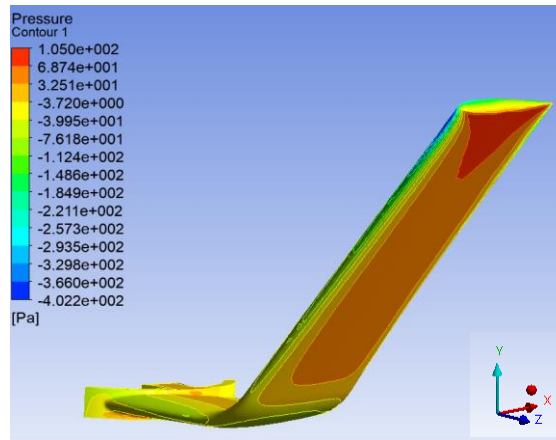
Figure 3.18. Wind load mapping.

As was stated earlier, the blades of this turbine will be treated as a cantilever beams. The loading case described in Figure 3.18 and Figure 3.19 denotes the load application for the static structural analysis. Though Figure 3.18 shows a pressure concentration at the tip of the blades the simulations will be done as a load affecting the whole face of the turbine blade as depicted in Figure 3.19. This was deemed acceptable since this method of load application will effectively overestimate the effect of wind on the blade.
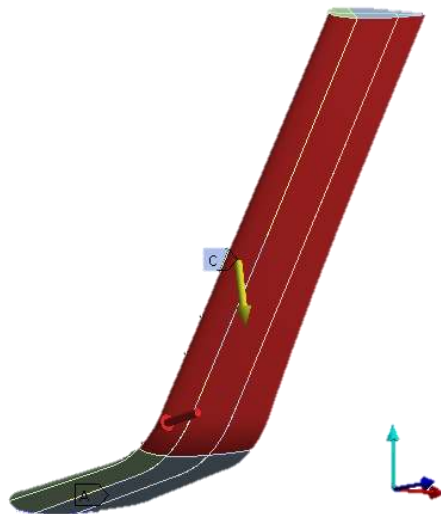
Figure 3.19. Analysis Settings with flapwise loading.

A medium unstructured mesh was developed for the span of each blade, where, solid tetrahedral (SOLID187 and SOLID186) elements are used. The root portions of blades designs 1 and 2 were meshed with solid hexahedral elements, and the thin features of the blade were meshed with SURF154. Blade 3 consisted of Hex20 and Wed15 elements.

3.11.2. Fatigue Analysis

The fatigue analysis was done at 8 m/s wind speed. The rationale behind this decision was to assess the fatigue criteria under the design wind speed (8 m/s) in order to judge the longevity of the blade profiles. These conditions for this design would be considered normal operation.

The Goodman fatigue theory was applied for this analysis, it is expressed by the equation in *(7)*. In general, most experimental data falls between the Goodman and Gerber theories with the Soderberg theory usually being overly conservative. The Goodman theory can be a good choice for brittle materials with the Gerber theory usually a good choice for ductile materials (Browell and Hancq 2006). The loading for our analysis was fully reversed.

$$\frac{\sigma_{Alternating}}{S_{Endurance\_Limit}} + \frac{\sigma_{Mean}}{S_{Ultimate\_Strength}} = 1 \qquad (9)$$

The loading for this project was set to zero-based since the simulation being targeted is the effect of centripetal force on the rotor blades as a cyclical load, in the same way it would occur as the turbine rotates to produce energy.

3.11.3. Modal Analysis

In a modal analysis, since we are usually interested only in the natural frequencies and the relative shapes of the vibration modes (the absolute values of deformation depend on the energy that excites the structure), the damping effect is usually neglected.

$$[M]\{\dot{D}\} + K\{D\} = 0 \qquad (10)$$

It is this equation that ANSYS Workbench solves in a Modal analysis system. Note that

modal analysis is a linear analysis; all nonlinearities are ignored (Lee 2017).

For modal analysis six Eigen modes were studied to analyze the most likely response that

the turbine blades would have. The frequencies 1 to 6 are analyzed by fixing the section of the

blade considered to be the root in each design, and observing the total deflection in each frequency.

	Blade 1			Blade 2			Blade 3		
	Structural	**Fatigue**	**Modal**	**Structural**	**Fatigue**	**Modal**	**Structural**	**Fatigue**	**Modal**
Element	318610	371112	454710	216839	3258	3258	1296	1920	1920
Nodes	498880	747836	125699	364682	1480	1480	7716	9776	9776
Skewness	0.95	0.951	0.926	0.949	0.93	0.93	0.875	0.816	0.815
Element type	TET10, HEX20, WED15, PYR13	TET10, HEX20, WED15, PYR14	TET4, HEX8	TET10			HEX20		

Table 3.7. Summary of mesh statistics for structural study.

Table 3.7 displays the mesh statistics for all three structural cases being analyzed. The

instances where a large number of mesh elements are presented, represent the instances in which

a fine mesh elements were used. This was done to account for small details in each geometry or

instance of analysis.

3.11.4. Static Rotor Analysis

ANSYS CFX solver was set to calculate the effects of wind flow in a steady state

stationary flow field. The static conditions analyzed here are setup where the turbine is open to

flow and laid out as demonstrated in Figure 3.20. The walls of the field are
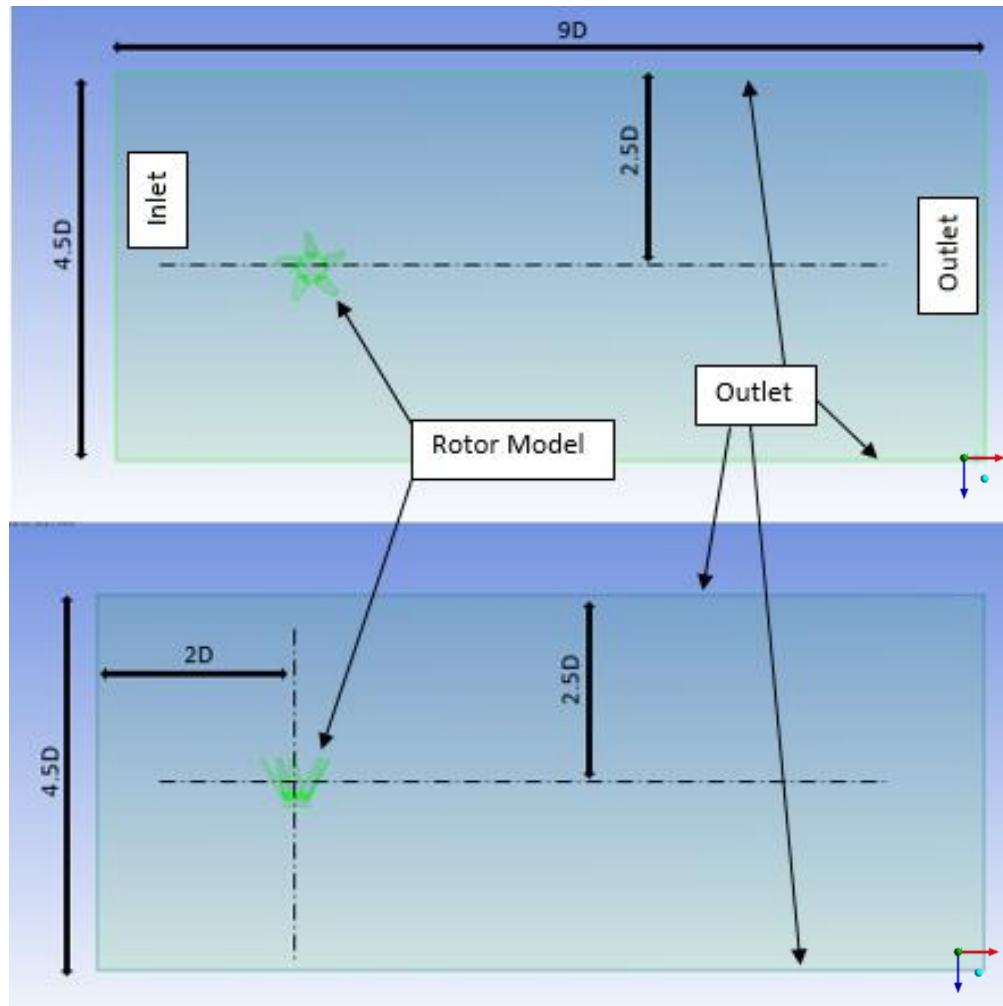
Figure 3.20. Three-dimensional computational domain for static conditions.

Denoted in Figure 3.20 is the static flow field. The flow field is described in terms of the rotors diameter. These dimenstions allow for the flow to become fully developed and allow adequate spacing for reactions within the field to be displayed fully. One case of the mesh is displayed in Figure 3.21. Notice from the figure the inflation layers that were established to surround each blade in order for ANSYS to better estimate the behavior of fluid with the blades surface.
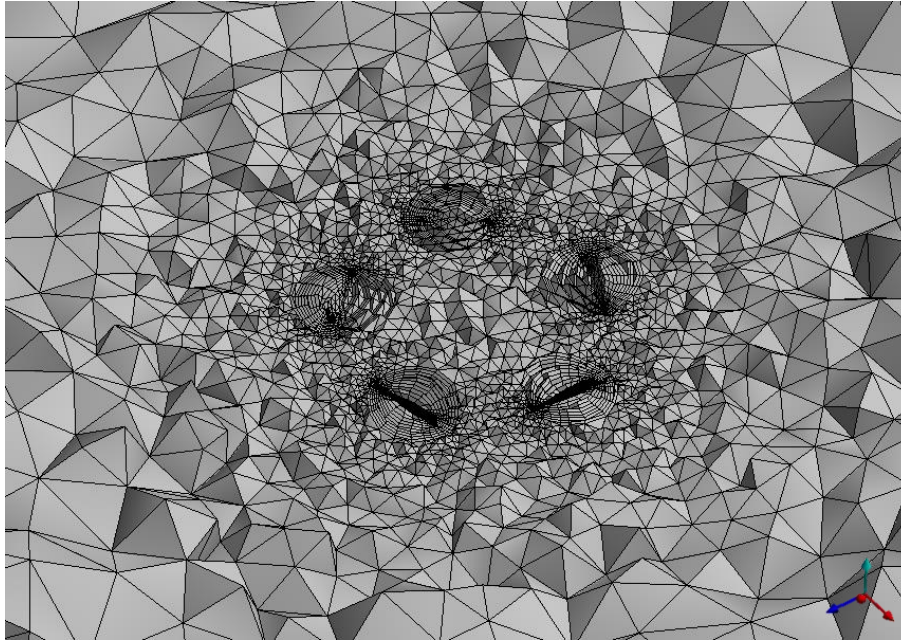
Figure 3.21. Static Structural Cut-away of mesh.

The inflation layers serve as a means of further discretizing the simulation field so as to infer the characteristics of wind interaction with the blades more accurately.

	3B45D	**5B45D**	**5B45D (5deg)**	**5B60D**
Element	323916	404200	479290	512087
Nodes	91345	167460	115939	184956
Skewness	0.93	0.95	0.922	0.961
Element type	TET4, WED6, PYR5	TET4, WED6, PYR5	TET4, WED6, PYR5	TET4, WED6, PYR5

Table 3.8. Summary of mesh statistics for static aerodynamic study.

The summary of mesh statistics for the aerodynamic study is encapsulated in Table 3.8. Medium mesh settings were applied for all cases.

Boundary conditions for the simulations are taken from experimental data. These include air velocity and inlet speed and corresponding rotational speed of the blades. The pressure outlet is kept at constant atmospheric pressure. The blade walls are given a no slip condition (Salyers 2016).

3.11.5. Transient Dynamic Rotor Analysis

The CAD models are imported into ANSYS Design Modeler, and fluid regions are added to the geometry. For transient three-dimensional analysis of VAWTs, two separate fluid domains are needed for simulation (Alaimo, et al. 2015). A sphere 15 inches in diameter is enclosed around the model and is established as a rotating zone. A second zone which will be stationary and represent the far field fluid flow domain is created with a rectangular box enclosure. The dimensions of the transient rotor analysis are established identical to the static. The entire three-dimensional computational domain is described in Figure 3.22.
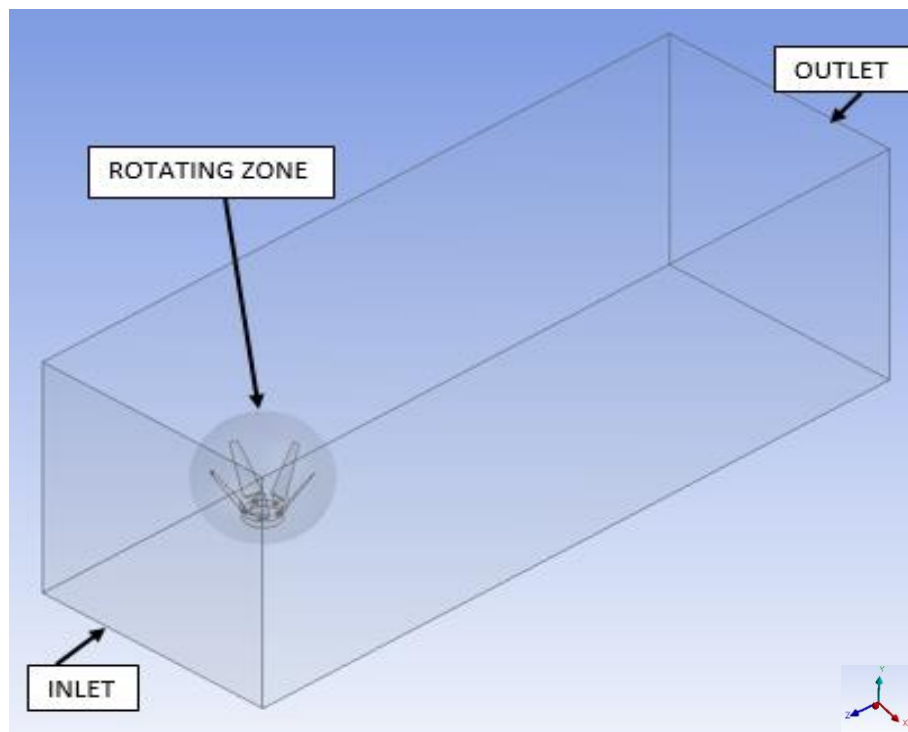
Figure 3.22. Three dimensional domain of moving mesh.
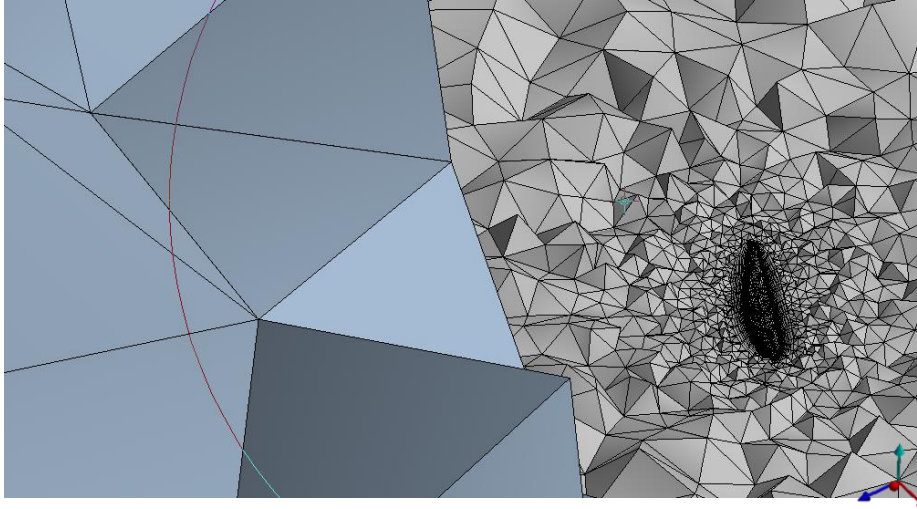
Figure 3.23. Section view of transient mesh.

A sectional view of the mesh used in the transient dynamic flow study is included in Figure 3.23. This figure displays the mesh variation betweenthe fluid zone and the rotating zone. As well as the inflation layers around the blade profile. The inflation layers serve as a means of further discretizing the simulation field so as to infer the characteristics of wind interaction with the blades more accurately.

A mesh interface is created between the two zones. The interface is necessary because the nodes on the boundaries of the far-field and rotational zones are intentionally non-conformal. The interface pairs these so that interpolation can occur, and fluid may pass into and out of the rotating region (Salyers 2016).

	3B45D		5B45D		5B45D (5deg)		5B60D	
	Static Transient	**Dynamic Transient**	**Static Transient**	**Dynamic Transient**	**Static Transient**	**Dynamic Transient**	**Static Transient**	**Dynamic Transient**
Element	323916	498135	404200	457340	479290	434197	512087	2629624
Nodes	91345	724318	167460	172078	115939	293447	184956	498262
Skewness	0.93	0.946	0.95	0.91	0.922	0.95	0.961	0.954
Element type	TET4, WED6, PYR5	TET4, WED6, PYR5	TET4, WED6, PYR5	TET4, WED6, PYR5	TET4, WED6, PYR5	TET4, WED6, PYR5	TET4, WED6, PYR5	TET4, WED6

Table 3.9. Summary of mesh statistics for transient aerodynamic study.

The summary of mesh statistics for the aerodynamic study is encapsulated in Table 3.10. Medium mesh settings were applied for all cases.

Boundary conditions for the simulations are taken from experimental data. These include air velocity inlet speed and corresponding rotational speed of the blades. The pressure outlet is kept at constant atmospheric pressure. The blade walls are given a no slip condition and zero rotational velocity relative to the sliding mesh zone (equal to the rotating fluid domain) (Salyers 2016).

3.12. Turbulence and Flow Model

Standard k–ε (SKE) model is the most widely-used engineering turbulence model for industrial applications. This model is robust and reasonably accurate and contains sub-models for compressibility, buoyancy, combustion, etc. However, of course it has limitations,

- The ε equation contains a term which cannot be calculated at the wall. Therefore, wall functions must be used.
- Generally performs poorly for flows with strong separation, large streamline curvature, and large pressure gradient.

This is why in both instances of the fluid flow analysis (static and dynamic) the k-epsilon (K-ε) model is used along with a scalable wall function to determine the turbulence behavior within the fluid domain (FLUENT 2012).

3.13. Post Processing Data

After the simulations were run the data was processed using Excel 2013 software. The equations found in Section 3.12.1 were used for structural calculations, and the equations found in this section will be used to assess the aerodynamic performance. Once all simulations and

experimental results are obtained the main parameters that will be known are reactional torque from both experimental efforts and from numerical simulations, therefore, data processing must be done to compare the performance of the models to other research.

Non-dimensional coefficients are used for comparison to other similar research and validation of the experiment. Three of these universally used non-dimensional entities are considered for this study. The power coefficient describes the energy conversion efficiency of the turbine. Torque coefficient is a non-dimensional representation of rotor torque, which is proportional to power produced. Tip-speed ratio is defined as the ratio of the blade tip speed to the free-stream wind velocity (MacPhee and Beyene 2012).

In order to begin processing the data information about each turbines basic geometry are needed. The information detailed in Table 3.10, gives the basic parameters of each turbine rotor.

Rotor Swept Area	$A_s = DH$	(11)
Agular Velocity	$\omega = \frac{2\pi N}{60}$	(12)
Tip Speed Ratio	$\lambda = \frac{\omega D}{2V}$	(13)
Power	$P = T\omega$	(14)
Power Coefficient	$C_p = \frac{P}{\frac{1}{2}\rho AV^3} = \frac{T\omega}{\frac{1}{2}\rho AV^3} = \lambda Cm$	(15)
Torque Coefficient	$C_m = \frac{T}{\frac{1}{4}\rho ADV^2}$	(16)
Betz Limit Power	$P_{Betz} = \frac{1}{2}\rho A_s C_{p\_Betz}V^3$	(17)

Rotor	Height	Diameter	Area
3B45D	0.1798	0.414	~0.074
5B45D	0.1798	0.421	~0.076
5B45D	0.1798	0.421	~0.076
5B60D	0.217	0.329	~0.071
		Average	**~0.0743**

Table 3.10. Rotor Parameters.

Although we have calculated the average area to be about 0.0743 m^2 we will use 0.072 m^2 in all calculations for swept area. This will give a conservative estimate of all values and may also account for defects in the 3D printing process.

CHAPTER 4

RESULTS AND FINDINGS

4.1 Introduction

This chapter captures the results and discussions of all numerical and experimental data that was obtained in the execution of this work. The information will be organized in the following way:

- Firstly, the results from the structural analysis will be laid out. It will discuss all results from the methods lain out in Chapter 3, which includes, static structural, results of each blade design for 50 year parked rotor condition, moment reactions, response to aerodynamic loading, fatigue and modal analysis.

- The chosen blade geometry will be optimized based on the data obtained in areas where it is lacking and reassessed.

- The chosen geometry will be used to construct a rotor assembly. The assembly will also be assessed in the same manner, and the results presented.

- The aerodynamic rotor models are established based on the chosen blade profile and numerical torque is calculated for all models in varying wind conditions.

- The corresponding torque data is used to calculate corresponding torque and power coefficients for both static and dynamic conditions.

- Best rotors models are fabricated and tested experimentally in static conditions.

- Numerical and experimental results are compared and discussed.

4.2 Structural Results

4.2.1 Static Structural Results

Comparing the effects of wind on the three blade designs there was an identifiable increase in Maximum Equivalent stress as well as deformation. In general, for equivalent stress, values ranged between 1.26MPa and 17.72MPa. The data shows that from blade 1 the stress was from 1.26 to 17.72 MPa, for blade 2, 1.49 to 15.21 MPa and for blade 3, 2.27 to 13.05 MPa which were all well below the specified material limit of 71.5MPa for ABS plastic. Blade 1 proved to have the largest stress concentration of all the models depicted in Figure 4.1. Figure 4.2 depicts the displacement in each blade profiles.
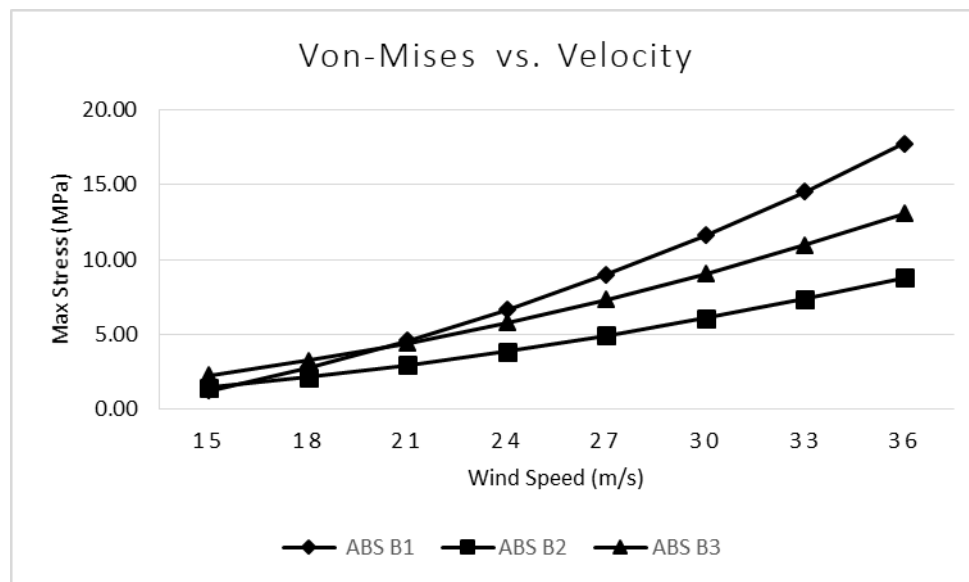

Figure 4.1. Flapwise Maximum Von-Mises Stress at various wind speeds.
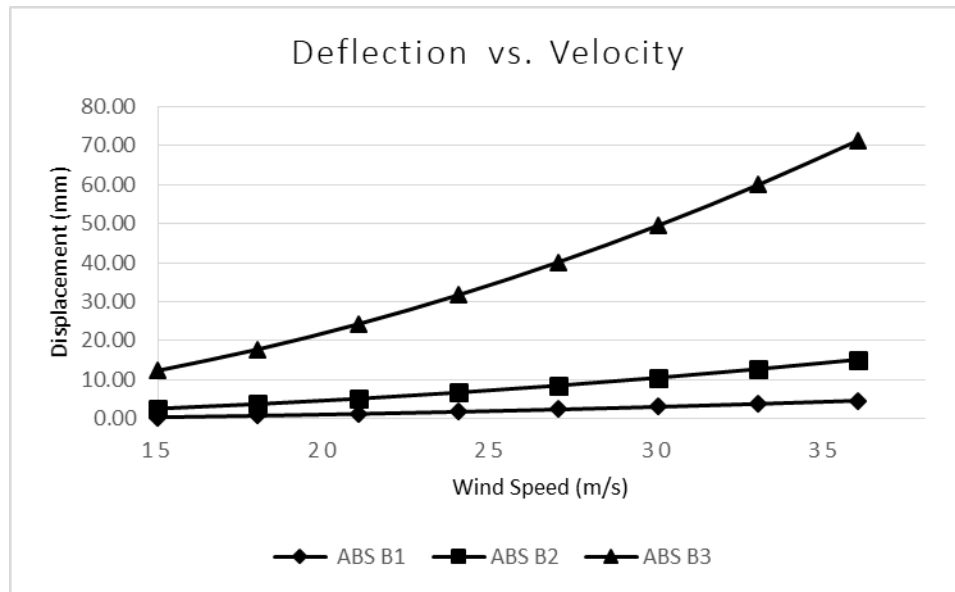
Figure 4.2. Flapwise Displacement at various wind speeds.

Blade 3's design showed consistently the largest displacement over the course of the wind rage with its minimum deflection that was about 2.82% (12.9 mm), and a max of 15.62% (71.4 mm) of the blades overall length. The other blade models being studied seemed to keep a more stable deflection ranging from 0.09% (0.42mm) to 1.02% (4.66mm) and 0.577% (2.64mm) to 3.33% (15.21mm) of the blades overall length for designs 1 and 2 respectively. Blade designs 1 and 2 were deemed acceptable since the deflection experienced by these designs were less than the 10% of overall blade length throughout the entire wind range criteria initially established. Blade design 3, however, violated this standard. Blade 1, 2 and 3 showed a minimum factor of safety of 2.60, 6.07 and 3.63 at 36 m/s respectively. The effect of gravity was only assessed on blade design 1 and added about 2 to 10 % to the overall Von-Mises result and did not seem to have a significant effect on displacement. Therefore the effect of gravity was deemed negligible and it was not included in the analysis of any of the other blades. This minimal effect of gravity was expected since the turbine size is small.
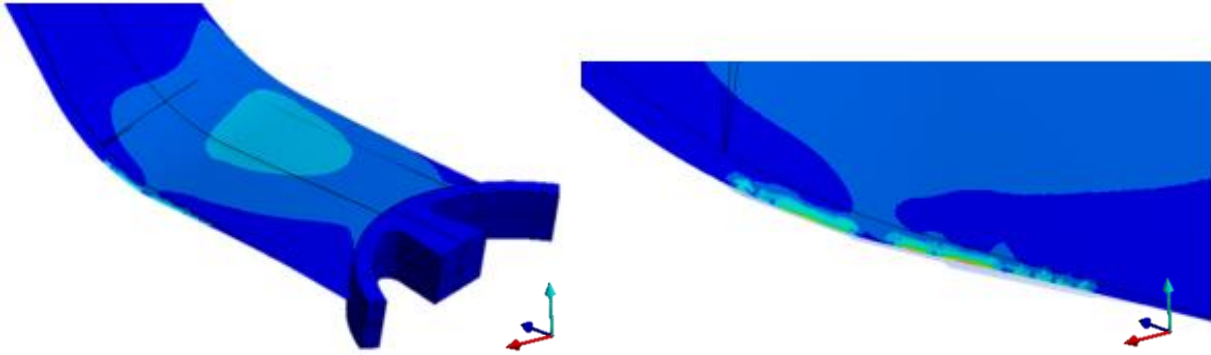
Figure 4.3. Blade 1 Von-Mises Stress at 15 m/s (left). Blade 1 Stress localization on trailing edge (right).
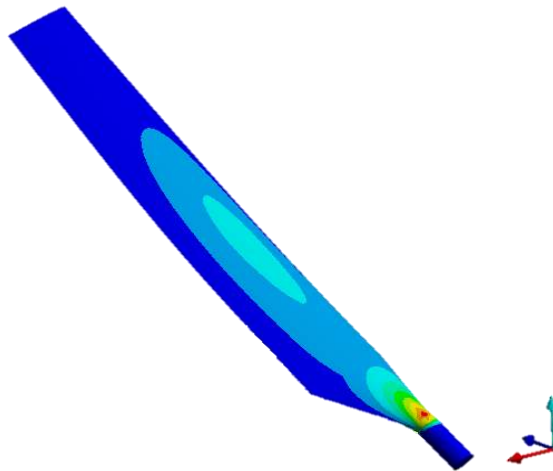
Figure 4.4. Blade 2 Von-Mises Stress at 15 m/s.

There is a critical stress value appearing in the trailing edge of blade 1. The stress distribution maps for blade designs 1, 2 and 3 can be seen in Figure 4.3, Figure 4.4 and Figure 4.5. Observe the stress localization happening along the trailing edge in blade 1. This behavior is common in wind turbines with airfoil shaped blades and can lead to catastrophic failures or at the very least a drastic reduction in aerodynamic efficiency (Marín, et al. 2009).
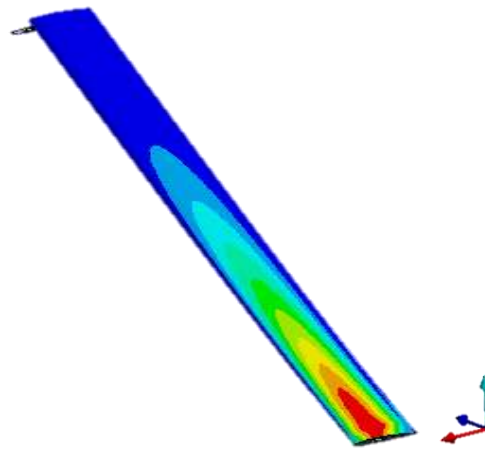
Figure 4.5. Blade 3 Von-Mises Stress at 15 m/s.

In order to get a better understanding of how each blade is responding to the wind the bending moment in each blade was assessed in terms of the same pressures used to load the blades for deflection and equivalent stress. This is illustrated in Figure 4.6. Note that the bending moment being assessed is at the root of each blade design, where they would be connected with the hub.
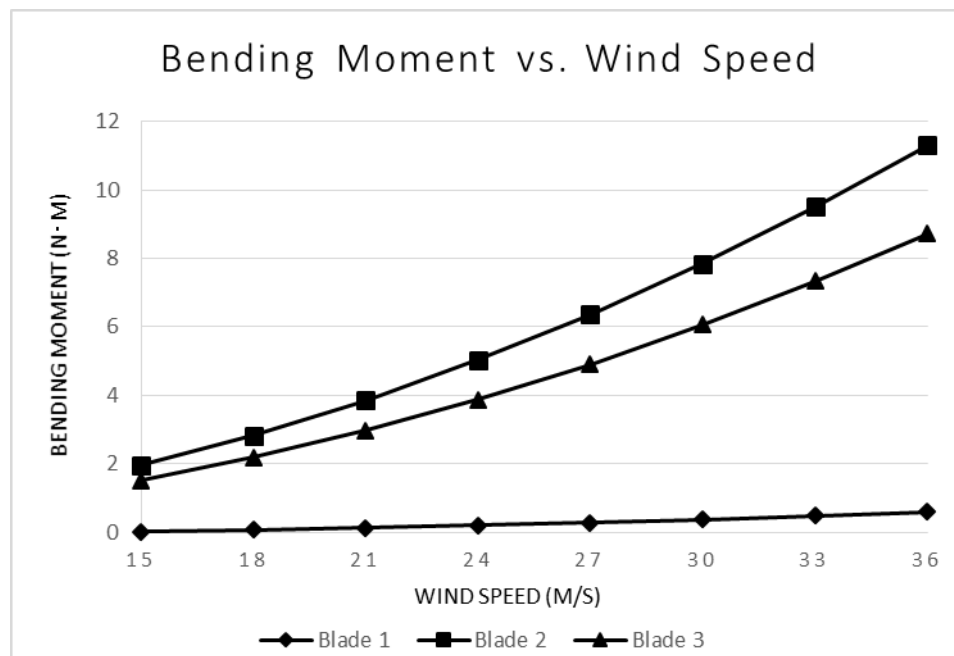
Figure 4.6. Bending moment at blade root at various wind speeds.

Taking the bending moment reactions at the root it was found that over the whole wind range blade 2 suffered the highest bending moment, of between 1.96-11.31 N·m.

The centrifugal force from equation *(8)* plays an integral part in the longevity of a wind turbine blade, as the rotor turns this force is consistent at the root of the blade, and is variable with wind speed as can be seen from Figure 4.7. That being the case, this force created as a result of rotation was also statically assessed, for each blade throughout the wind range.
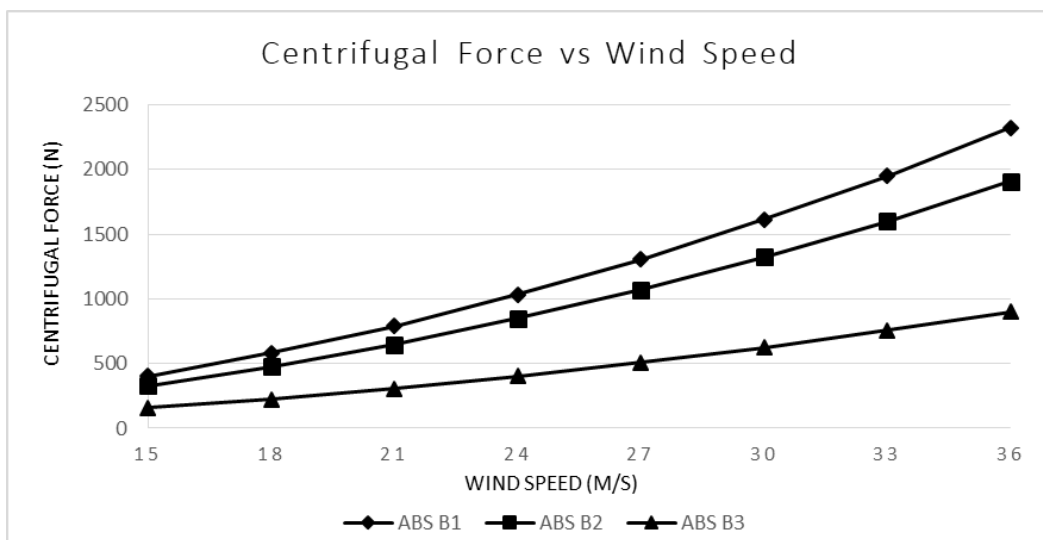
Figure 4.7. Centrifugal force through the wind range.

The highest centrifugal force observed was experienced by blade 1, and the lowest by blade design 3. This can be attributed to the fact that the design of blade 1 is more robust that the other two and has a greater mass (Table 4.1). Since the centrifugal force an object will create is a function of its mass this data is cohesive.

Design	ABS (KG)
B1	0.67
B2	0.55
B3	0.26

Table 4.1. Mass of each blade design.

4.2.2 Fatigue Analysis Results

The fatigue analysis (Table 4.2) revealed that mostly all the designs have more than sufficient longevity as can be seen from the life criteria reported in hours of life. This could be attributed to the fact that the loads were very small compared to the geometries and the material they are acting upon.

Design	Fatigue @ 8 m/s			Fatigue @ 15 m/s		
	Equiv. V-M (MPa)	Min. FOS	Avg. Life (hrs)	Equiv. V-M (MPa)	Min. FOS	Avg. Life (hrs)
B1	-	0.044	0	-	.0127	0
B2	19.59	2.56	1.45E+11	14.82	0.44	1.46E+10
B3	18.87	2.66	9.17E+10	6.36	0.76	1.32E+10

Table 4.2. Fatigue Analysis results.

The results obtained from the fatigue analysis shows that blade design 2 holds the highest stress response, at both the normal operating speed (8 m/s) outperforming blade 3 by 3.74% and what would be considered extreme case in terms of fatigue (15 m/s), outperforming blade design 3 in this instance by 79.89%. Therefore, blade design 2 will tolerate more stress before failing due to fatigue. From the three design cases it can also be noted that blade design 2, in each case outperforms the other blades in average life by 45% in normal conditions and by 10% in the extreme condition. The study goes on to show that there will be a catastrophic failure in blade design 1 within the first few iterations leading to a safety values well below a factor of safety of 1 in both instances. Blade designs 2 and 3 both achieved a FOS value of greater than 1.5, as reported in Table 4.2. Equivalent stresses were not recorded for blade design 1 since the software reported that the design would fail. The failure of blade design 1 can be observed from the factor of safety distribution along the blade (Figure 4.8).
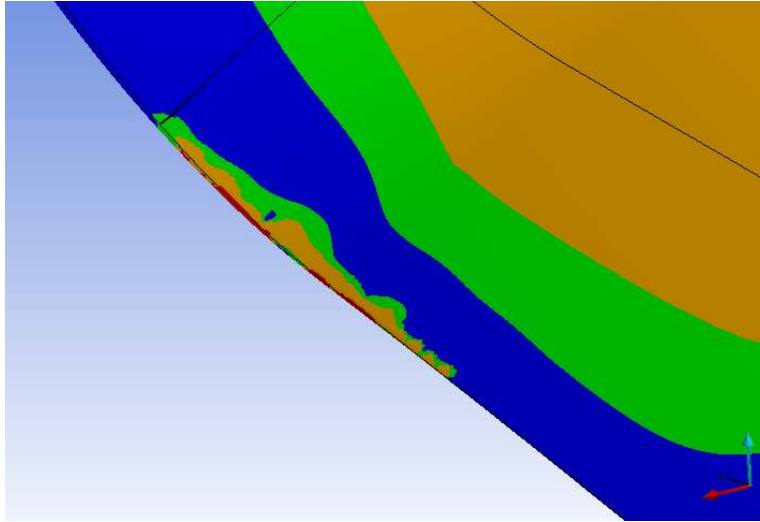
Figure 4.8. Factor of safety distribution Blade 1.

Although this result reflect that there would be a failure region in the trailing edge of blade 1, this result could be due to the FEA tool (ANSYS 19.1) having issues processing geometries with very small thickness. A greater cause for concern would be the region depicted as having failed due to the fatigue stresses at 15 m/s in blade 1 (Figure 4.9).
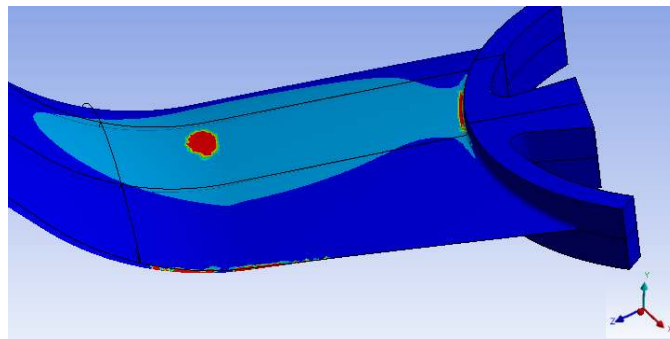
Figure 4.9. Blade Life showing damage at 15 m/s.

Figure 4.9 depicts the blade life result and also shows major issues arising in the fileted corner where the blade meets the mounting apparatus, in the trailing edge and a very large area of failure in the shoulder of the blade.

4.2.3 Modal Analysis Results

The modal analysis was done as a final step to determining which blade would be chosen for optimization and move on to become the blade profile use in the test model for aerodynamic study. The first six blade modes in each design case were taken for analysis as these proved to be sufficient for the study. The results are depicted in Figure 4.10, Figure 4.11 and Figure 4.12.
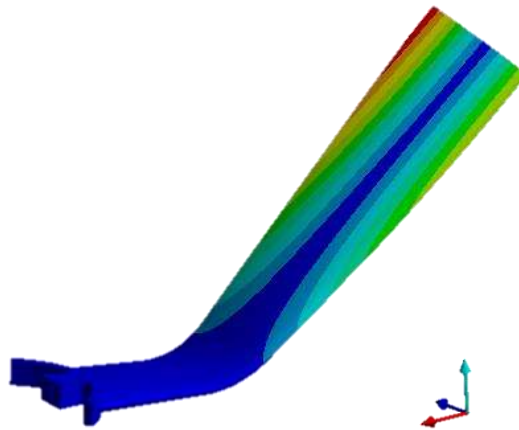
Figure 4.10. 5th mode of blade 1.
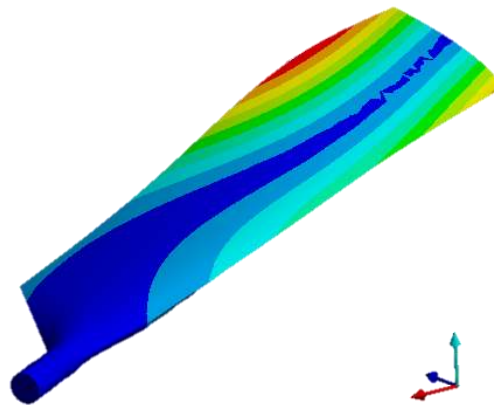
Figure 4.11. 5th mode of blade 2.
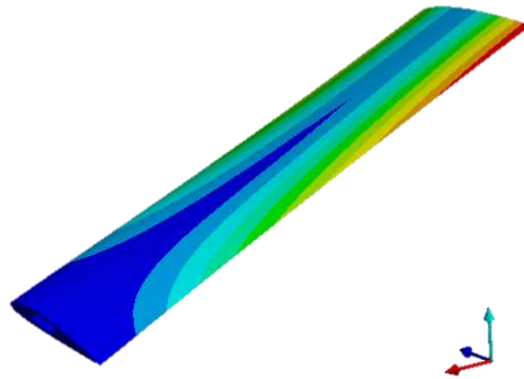
Figure 4.12. 4th mode of blade 3.

In each blade the motion of the blade twisting or experiencing torsion about its planform area was the mode that gave the most cause for concern. The frequency values of the blade modes that cause the largest displacement were 397.61 Hz (5th mode), 178.01 Hz (5th mode) and 123.37 Hz (4th mode), for blades 1, 2 and 3, respectively. Though these were not the highest frequencies in the range, they are quite large and the likely hood of any of the blades getting to these frequencies under normal operation is unlikely. The deformation experienced as a result of modal analysis are 446.82mm, 207.74mm and 203.25mm for blade 1, 2 and 3 respectively.

Overall, Blade design 2 had the best results based on all the criteria set. The design showed an excellent Von-Mises stress response that was well below the yield strength of the material at 15.21MPa for static structural which achieves a FOS of 4.7 and 19.59MPa for fatigue which gives a factor of safety of 2.56 at normal design speed of 8 m/s. A maximum deflection at 36 m/s of 3.33% of the blades overall length (18 inches) was achieved. The Centrifugal force was also low throughout the wind range due to the blades lighter blade profile design. The design had the highest stress of all three designs during fatigue loading which tells us that it will endure a higher load before it succumbs to failure by fatigue stress.

This blade did, however, present some issues of concern. For example, though this blade experiences the lowest Maximum Von-Mises stress, it experiences the largest moment reaction from the blade root due to wind of all three blade designs.

4.2.4 Optimizing Chosen Blade

Blade design 2 optimized to reduce the effects of bending moment for experimental testing. The optimized blade profile can be seen in Figure 4.13. It was hypothesized that by adding a thicker blade root and moving the placement of the blade root closer to the center of pressure of the airfoil shape there should be better response to bending stress.
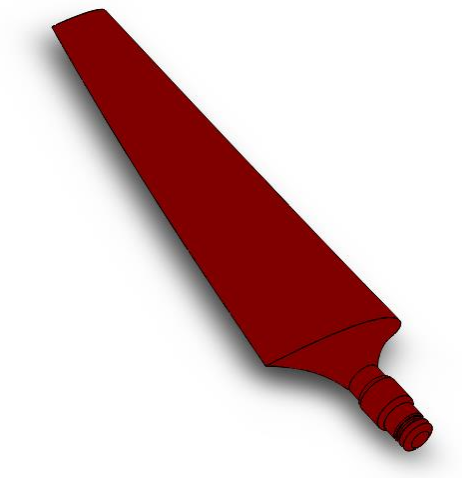
Figure 4.13. Optimized blade design.

Depicted in Figure 4.14 is the test rotor model anatomy. The test rotor is about half the size of the model used for structural analysis, therefore, reasoning follows that this blade will not be able to handle the same amount of loads as the larger model.
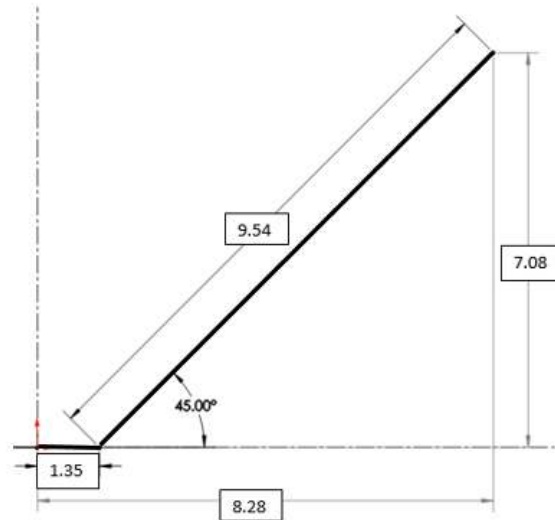
Figure 4.14. Schematic of intended test blade.

This test model will only experience winds up to about 13m/s based on the parameters of the subsonic wind tunnel that will be used in the experimental section of the study. Therefore, the lower end of the structural analysis design wind range (15 m/s) will be taken to analyze the test blade.

4.2.5 Structural Verification of Chosen Blade

A more robust blade root design was employed as well as a more aggressive taper in chord length from blade tip to root, in order to reinforce the structural capacity of the blade's root, overall blade geometry and any subsequent turbine rotors. The optimized design was tested at 15 m/s and using equation *(4),* a force of 1.26N was obtained. The numerical tests showed that the resulting displacement in the blade was 0.278 mm (0.01in) which is 0.1% of the overall blade length, equivalent stress of 0.802MPa, a FOS of 15 and bending moment was 0.15 N·m for the static structural analysis. The fatigue analysis of the blade yielded a safety factor of 15, an alternating equivalent stress of 0.401MPa and a design life of 1.46E+11. The centrifugal force experienced in the design was 67.88 N, calculated from equation *(8).* This force was applied as a zero-based

fatigue load in order to simulate the loading of the blade as it spins. The minimum life of the blade as a result is 1.76E+10 hours, FOS is 2.29 and Equivalent alternating stress is 21.86MPa. A rotor model was then established from the blade profile (5-bladed with 45 degree inclination angle), and tested in the same way (Figure 4.15) to compare the results.
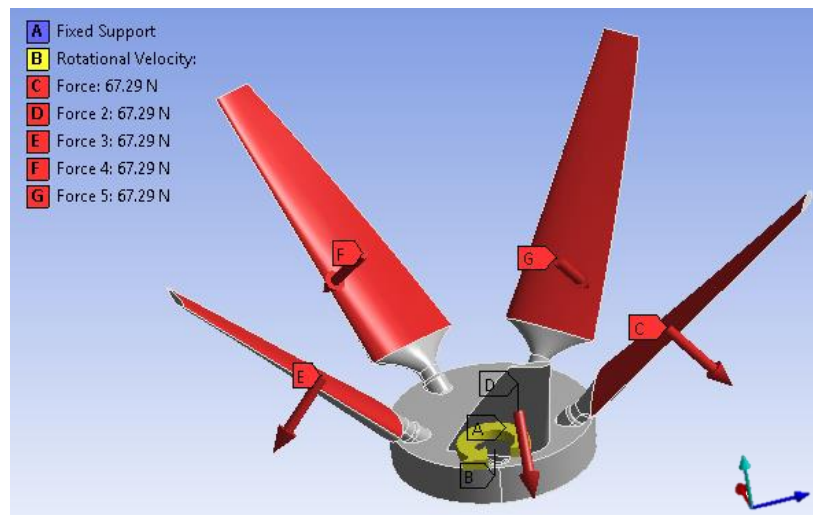
Figure 4.15. Structural Boundary Conditions on test Rotor.

As can be seen in Figure 4.15 the aerodynamic resultant force is being assessed at 15m/s where a conservative estimate of rotation was set at 500 RPM. The resulting fatigue response from this final structural verification of the turbine rotor, is as follows: FOS is 1.87, Equivalent alternating stress is 16.91MPa and a life of 1.02E+10 hours. It is noted from Fig. of the equivalent stress, that the concentrations occur in the same place and from table are in relatively close agreement.

Component	Deformation (mm / in)	Equivalent Von-Mises (MPa)	Factor of Safety (FOS)
Rotor	16.69 (0.657)	16.91	1.87
Blade	15.01 (0.591)	21.86	2.29
Percent Diff. (%)	10.59	25.54	20.19

Table 4.3. Test model validation.

Notice from Table 4.3 the deformation of the rotor vs the single blade is 10.59% more, which can be attributed to the rotational velocity that was added. The stress, however, is 25.54% less in the rotor model than in the blade model. This difference was attributed to the way the rotor design was modelled in ANSYS in order to carry out structural analysis. Notice from Figure 4.15 that for simplification of the scenario the blades and hub is modelled as one solid piece rather than a hub with five separate blades. Therefore the way this problem is expressed may account for why the rotor and blade models have a slight disagreement. There was also a 20.19% percent difference in the factor of safety obtained for the single blade vs the rotor assembly.

Figure 4.16. Equivalent Von-Mises Stress response on test Rotor and blade.
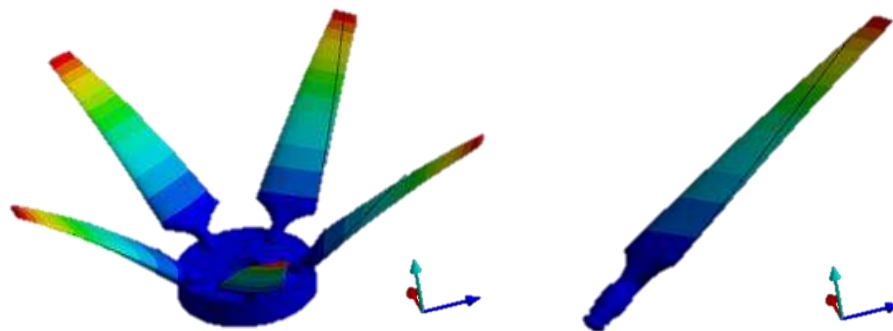
Figure 4.17. Deflection response on test Rotor and blade.

Figure 4.16 and Figure 4.17 illustrates the von-mises stress concentration and deformation occurring in the rotor assembly as well as the redesigned blade model. As expected the highest

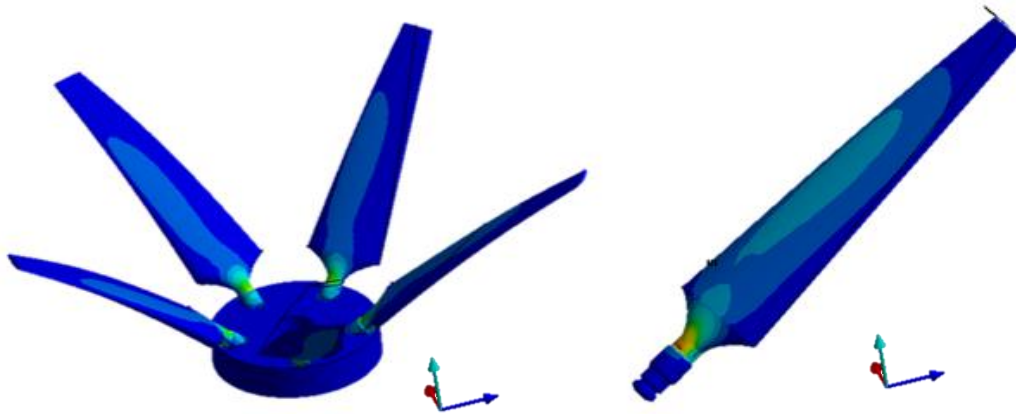concentration of stress occurs in the regions where the blade is anchored in at the root, in both the rotor and blade model. One side of the models is experiencing tension as a result of loading and the reverse side is experiencing compression. The largest deformation occurs at the tips of the blade. Modal analysis was not performed on the rotor since it is assumed that the results of this analysis would give a similar result as those obtained for the three initial blade designs. Also, and more importantly, it was already determined that the frequencies estimated by numerical study would not be seen by our models under real-world application. In the modal analysis the critical mode shapes would not be achieved at the low RPMs of this test design. The data discussed in this section was then used to fabricate eight rotor models. These rotor models will be further explored in the Aerodynamic study.

4.3 RPM Measurement Results

An initial transient analysis was carried out as expressed in Chapter 3 of this document. The results are detailed here. The transient analysis was done in an effort to obtain actual rotational speeds of each rotor. These values were necessary in order to establish the boundary conditions for the numerical study. The RPM measurements were taken as per the methods described previously in Chapter 3. The gathered experimental data was translated to angular velocity and is represented in Figure 4.18. Note that the data depicted in Figure 4.18 was also used in the determination of the static aerodynamic study as well.
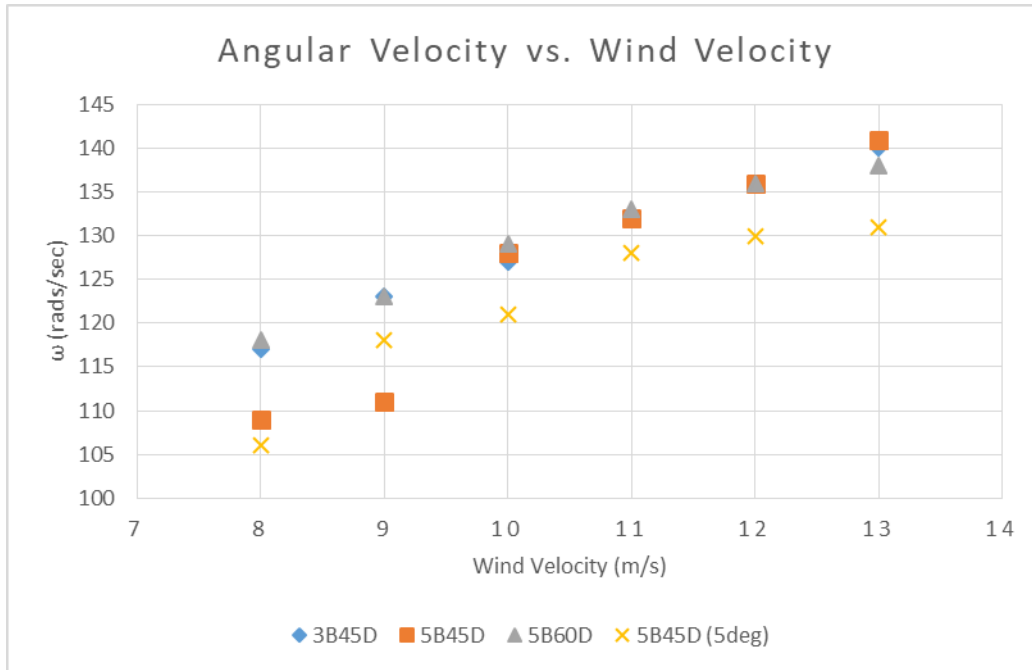
Figure 4.18. Experimental angular velocity vs wind velocity.

The summary of the collected data depicted in Figure 4.18 illustrates 5B45D (5deg) turbine rotor has the lowest angular velocity at 8 m/s followed by the 5B45D rotor. The 3B45D and the 5B60D rotor model exhibited a superior angular velocity at the start of the wind range, but is however matched by the 5B45D design from 10 m/s onwards. The 5B45D (5deg) maintained consistently the lowest angular velocity throughout the tested wind range except for at 9 m/s.

It should be noted that there is no load on the turbine as it rotates. The results of this dynamic performance, are from freely rotating rotors.

4.4 Aerodynamic Analysis Results

Eight rotor models were made they are listed and described in Table 4.4. The rotor assemblies developed all applied the same airfoils shapes as depicted in Figure 4.19. NACA 0040 was used from the start of the aerodynamic section of the blade to 50% the length of the blade section, then NACA 2414 was used on the remaining 50% of length. Once the rotor classifications

were established, they were tested numerically to assess their performance. This initial test was done at the design speed of 8m/s.

Rotor	# of blades	Inclination Angle	Blade pitch
3B45D	3	45	0
5B45D	5	45	0
3B60D	3	60	0
5B60D	5	60	0
3B45D	3	45	5
5B45D	5	45	5
3B60D	3	60	5
5B60D	5	60	5

Table 4.4. Test rotors classification.
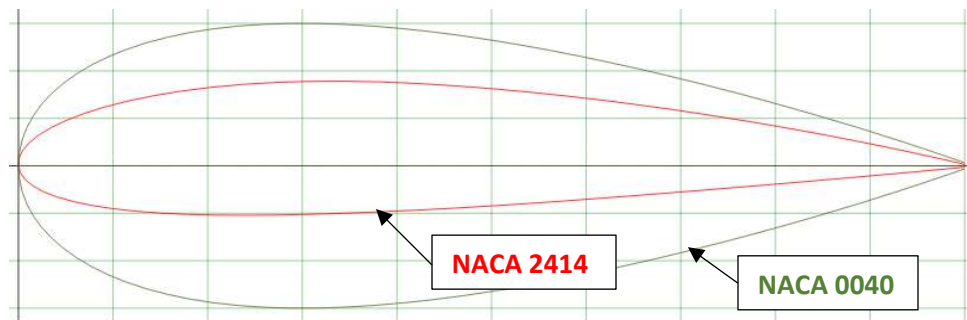
Figure 4.19. Airfoil description of all rotor models.

In Figure 4.20, the numerical torque values obtained from ANSYS finite element analysis tool is displayed. This data will give us insight into which rotors are performing at a more optimal level, from the perspective of reactional torque. Reactional torque was used as the determining factor since this torque production gives a good indication of which turbine rotors have the best self- starting capabilities at 8 m/s. In order to better visualize the reactional toque Figure 4.21 is created which displays the average values of each data set. This gives a good visual representation of where each turbine model stands.
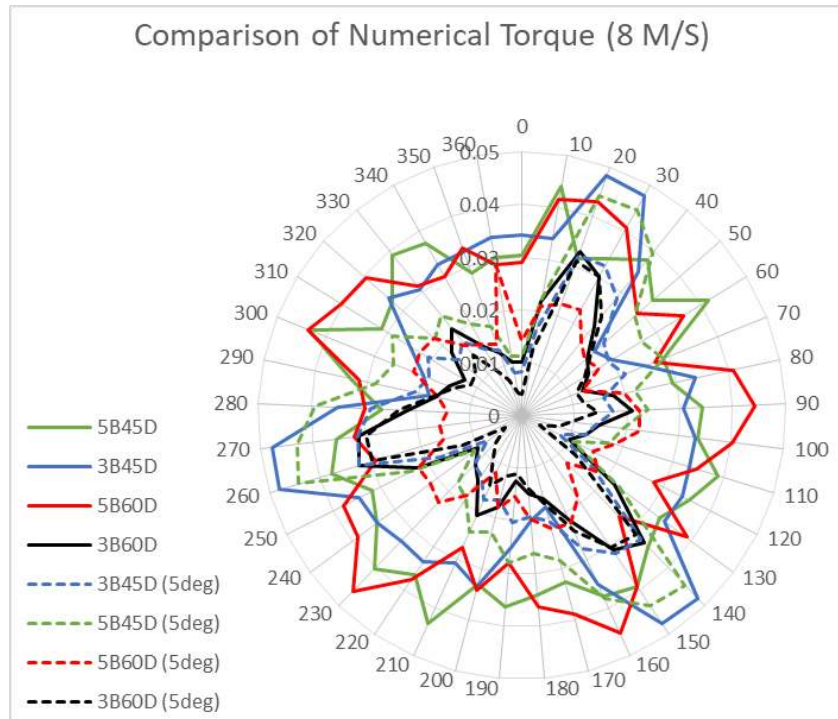
Figure 4.20. Comparison of established Rotor performance at 8m/s.

From the average numerical reactional torque (Figure 4.21) it can be observed that at 8 m/s the 3B45D, 5B45D, 5B60D and 5B45D (5deg), rotor assemblies have the best self-starting potential. Applying equations *(13)* through *(16)*, we can calculate the torque and power coefficient from these average reactional torque values in Figure 4.21. Observing these results as well it can be seen that the four rotor models cited previously, exhibit good potential. An average torque coefficient of 0.0591, 0.0554, 0.0599 and 0.0455, is presented for the 3B45D, 5B45D, 5B60D and 5B45D (5deg), respectively, and a power coefficient of 0.169, 0.159, .172 and 0.130, respectively at these corresponding torque coefficient values.
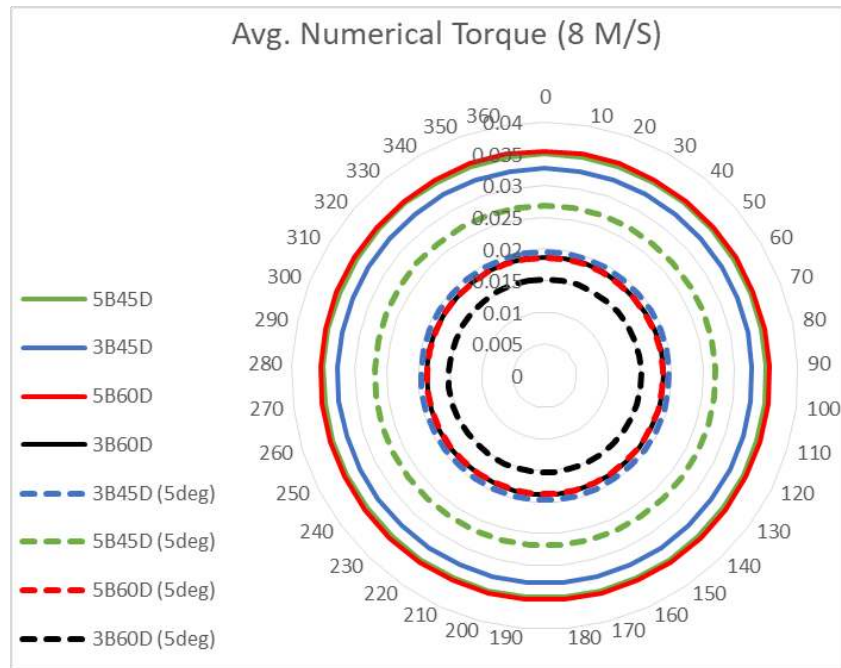
Figure 4.21. Comparison of established Rotor performance at 8m/s.

Observe from the torque diagram in Figure 4.20 that the number of blades on each rotor is evident from the torque graph. In general, all five bladed rotors experience a spike in 5 regions of rotation, namely, between 10-30, 80-100, 140-170, 210-230 and 300-320 degrees. Each three bladed rotor experiences this same spike in 3 regions, namely, between 20-30, 140-150 and 260-270 degrees. After performing these initial tests as was stated earlier the most underwhelming rotor models were discarded from the study. The best performing models will be examined in greater detail.

4.4.1 Static Aerodynamic Results

Displayed in Figure 4.22 is the numerical torque values as a function of azimuth angle for each turbine at 10 and 12 m/s, obtained from ANSYS 18.2 and 19.1. In each iteration of torque values from 8-13 m/s, the mean value of torque rose in each case. Please note that depicted in Figure 4.22 are the reactional torque vs rotational position results only for 10 and 12 m/s as 8m/s

is previously shown in Section 4.3 (Figure 4.20 and Figure 4.21). The maximum torque value achieved at 9m/s is around 0.076 Nm at 230 degrees by the 5B45D (5deg) rotor. This rotor is consistent in outperforming the other rotors through the entire wind range and achieves the highest torque values at 0.157 Nm at 300 degrees. The performance of the other rotors are generally grouped together around a mean value.
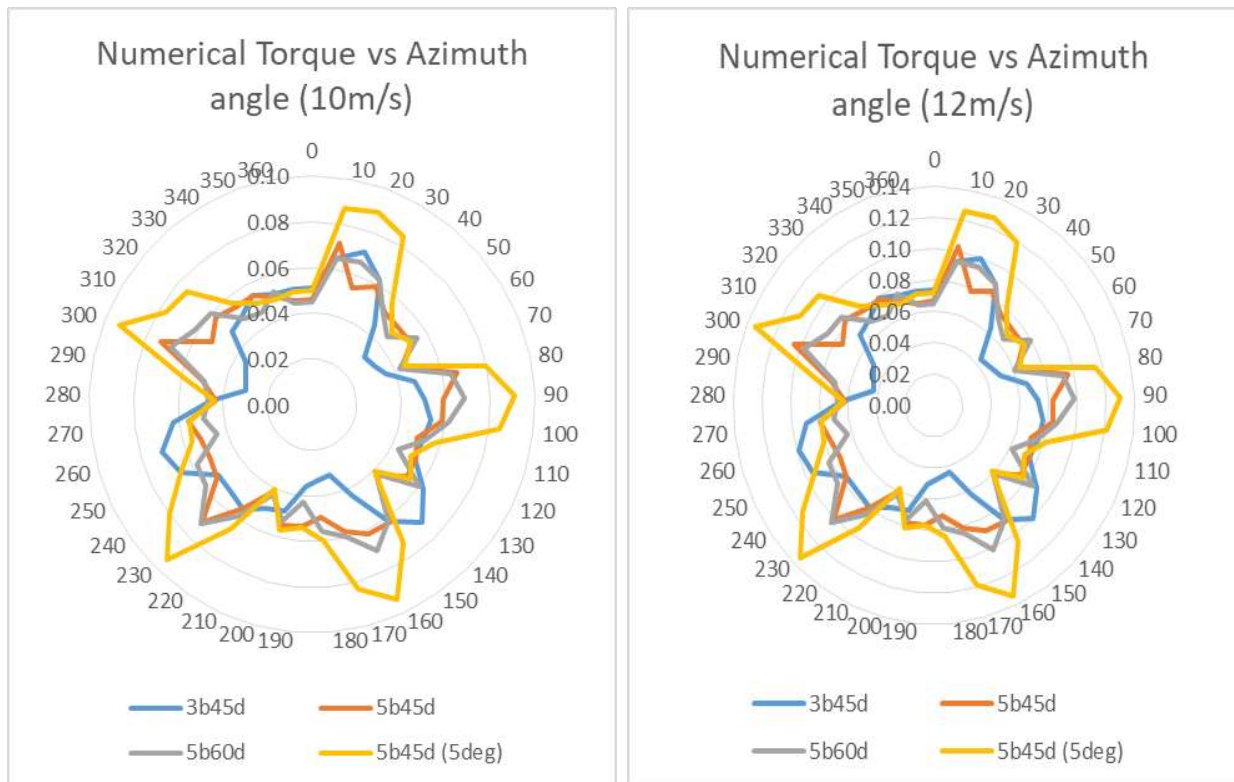
Figure 4.22. Numerical Torque vs. Azimuth angle at 10 m/s and at 12 m/s.

In Figure 4.23, Figure *4.24* and Figure *4.25*, the numerical torque coefficient versus azimuth angle for 8, 10 and 12 m/s, is illustrated. Once the torque coefficient is calculated we can see where 5B45D (5deg) has a wide spanning oscillation going from a low of 0.0185 at 120 degrees to a high of 0.0754 at 30 degrees, these values corresponded to a C_p value of 0.052 and 0.21. For numerical torque coefficient, beginning at 9 m/s and up to 13 m/s the general shape and magnitude of the torque coefficient versus azimuth angle graphs remain the same for all rotors. This indicates that

the torque response efficiency between these wind speeds generally remain constant among all the turbine models. From figure 28, the 5B60D had the highest torque coefficient values with the highest of 0.0987 at 240 degrees.
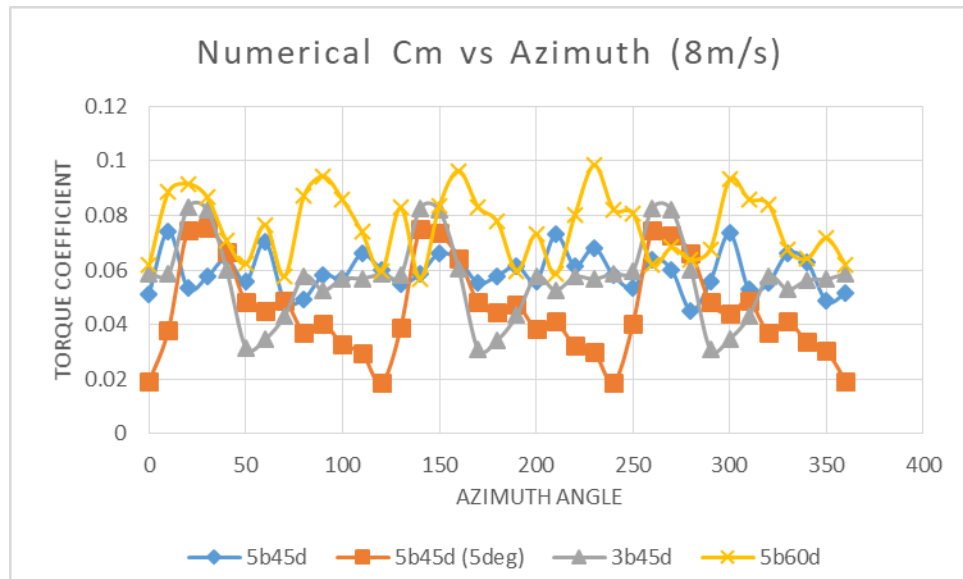
Figure 4.23. Numerical Torque coefficient vs. Azimuth angle at 8 m/s.
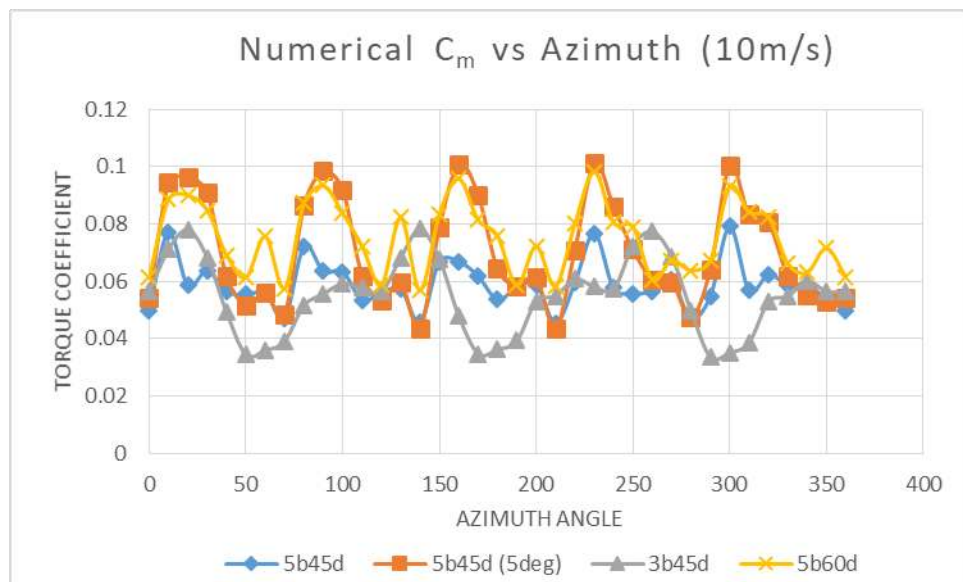
Figure 4.24. Numerical Torque coefficient vs. Azimuth angle at 10 m/s.
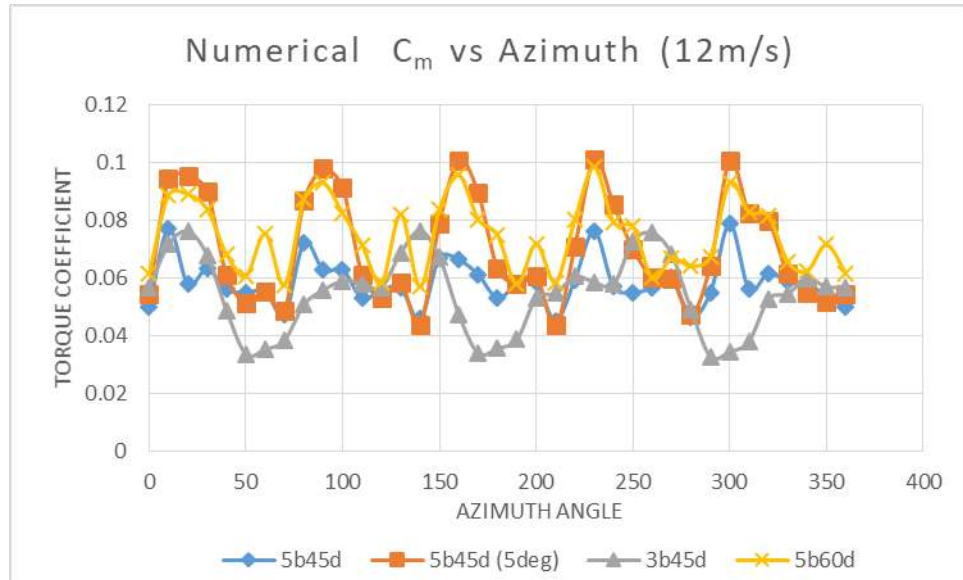
Figure 4.25. Numerical Torque coefficient vs. Azimuth angle at 12 m/s.

Figure 4.26 depicts the results of experimental torque at 8, 10 and 12 m/s. The first thing that can be observed about this data is that unlike the numerical data is that the data does not have identifiable peaks and valleys like that of the numerical efforts, the peaks and valleys do not give a clear indication of the number of blades used in each rotor case, as was the case with numerical data. Also, unlike the numerical data the experimental data shows the 5B45D (5deg) to be the worst performing rotor assembly and instead, the maximum performance experimentally was held by the 5B45D rotor.
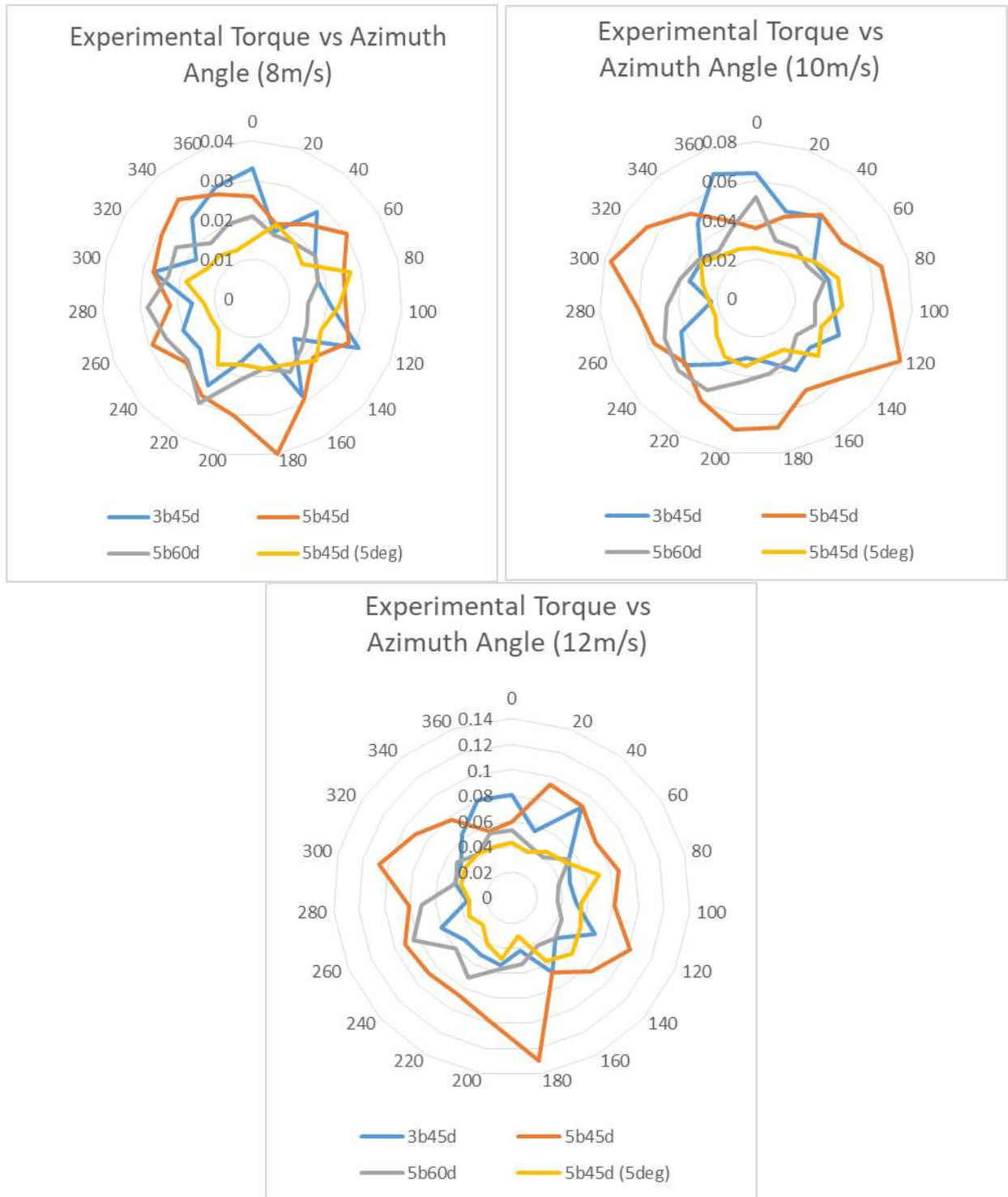
Figure 4.26. EXP Torque coefficient vs. Azimuth angle at 8 m/s, 10 m/s and 12 m/s.

The data obtained from the experimental efforts was processed and the mean and maximum

values recorded for both numerical analysis and experimental analysis then using equations *(11)*

through *(16)* the torque values derived are used to calculate torque coefficient and power coefficient. The data displayed in Table 4.5, illustrates this. Table 4.5, shows us the comparison of the different rotor assemblies in terms of their diameter, operating TSR, maximum recorded torque (C_m) and power (C_p) coefficient between a wind speed range of 8 to 12m/s.

Numerical					
Rotor	Diameter (m)	V (m/s)	TSR	C_m	C_p
3B45	0.414	8	3.0274	0.08291	0.25099
		10	2.6289	0.07826	0.20575
		12	2.3460	0.07634	0.17910
5B45D	0.421	8	2.8681	0.07430	0.21309
		10	2.6944	0.07918	0.21333
		12	2.3857	0.07885	0.18811
5B45D (5deg)	0.421	8	2.789125	0.07536	0.21018
		10	2.54705	0.10133	0.25809
		12	2.297958	0.10109	0.23052
5B60D	0.329	8	2.426375	0.09847	0.23894
		10	2.12205	0.09839	0.20879
		12	1.89175	0.09832	0.18331
Experimental					
Rotor	Diameter (m)	V (m/s)	TSR	C_m	C_p
EX-3B45	0.414	8	3.0274	0.05672	0.17170
		10	2.6289	0.07370	0.19374
		12	2.3460	0.06798	0.15949
EX-5B45D	0.421	8	2.8681	0.06760	0.19389
		10	2.6944	0.08653	0.23315
		12	2.3857	0.13000	0.23296
EX-5B45D (5deg)	0.421	8	2.789125	0.04563	0.12727
		10	2.54705	0.04759	0.12122
		12	2.297958	0.07100	0.12162
EX-5B60D	0.329	8	2.426375	0.06399	0.15527
		10	2.12205	0.07372	0.15643
		12	1.89175	0.08400	0.14846

Table 4.5. Static Results Summary.

Figure 4.27 illustrates the numerically derived torque coefficients from each turbine. The figure displays the numerical torque coefficient variation with the change of Tip Speed Ratio for each turbine. It can be noted that the torque coefficient achieved by the 5 bladed rotor with a 45 degree angle of inclination and 5 degrees of blade twist at a TSR of 2.54, was the highest torque coefficient achieved.
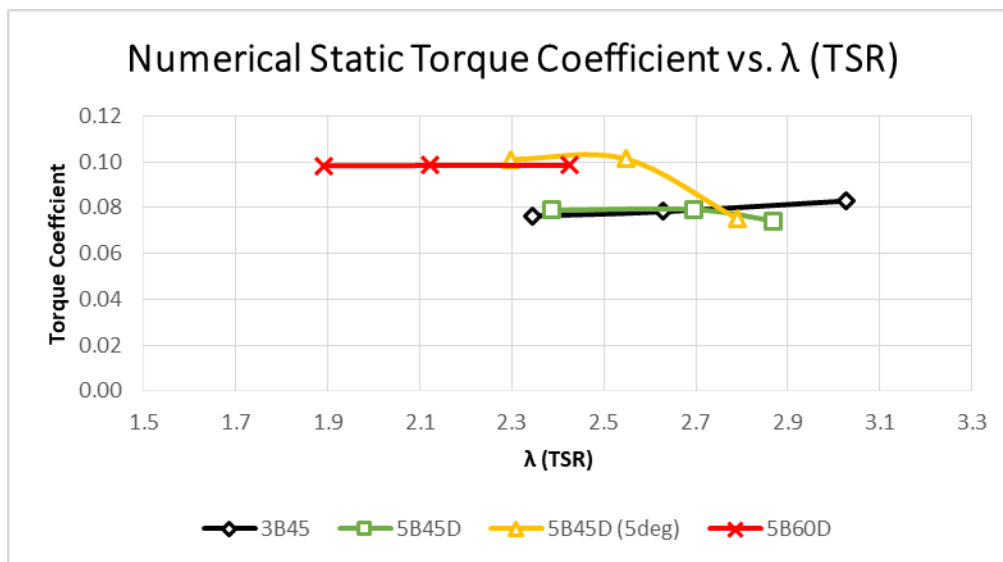
Figure 4.27. Numerical Torque Coefficient vs. TSR.

Figure 4.28 depicts the numerical power coefficient as a function of the TSR. It should be noted that at a TSR of 2.54 the highest power coefficient of 0.258 is achieved by the 5B45D (5deg) turbine rotor. Observe that the 5 bladed 60 degree rotor produces its power at a lower tip speed ratio (TSR) than the other rotor assemblies. The 3 bladed 45 degree rotor produces the second highest power coefficient of 0.251 at a TSR of 3.03. The 3B45D rotor also produces the lowest C_p in the series of 0.18 at TSR 2.35, overall the 3B45D operates over the largest TSR range.
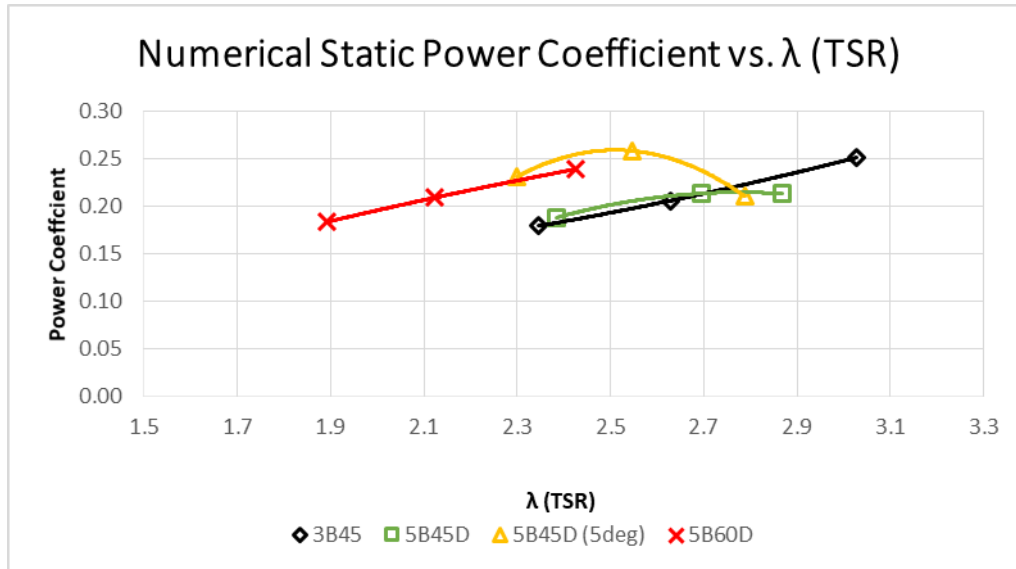
Figure 4.28. Numerical Power Coefficient vs. TSR.

Figure 4.29 and Figure 4.30, displays the combination of numerical results alongside the experimental results. The experimental results are labelled with the prefix 'EX' for clarity. The data for the 3 bladed 45 degree rotor assembly was the only data that appeared to be coherent for both numerical and experimental data. There was a maximum percent difference of 37.51%.
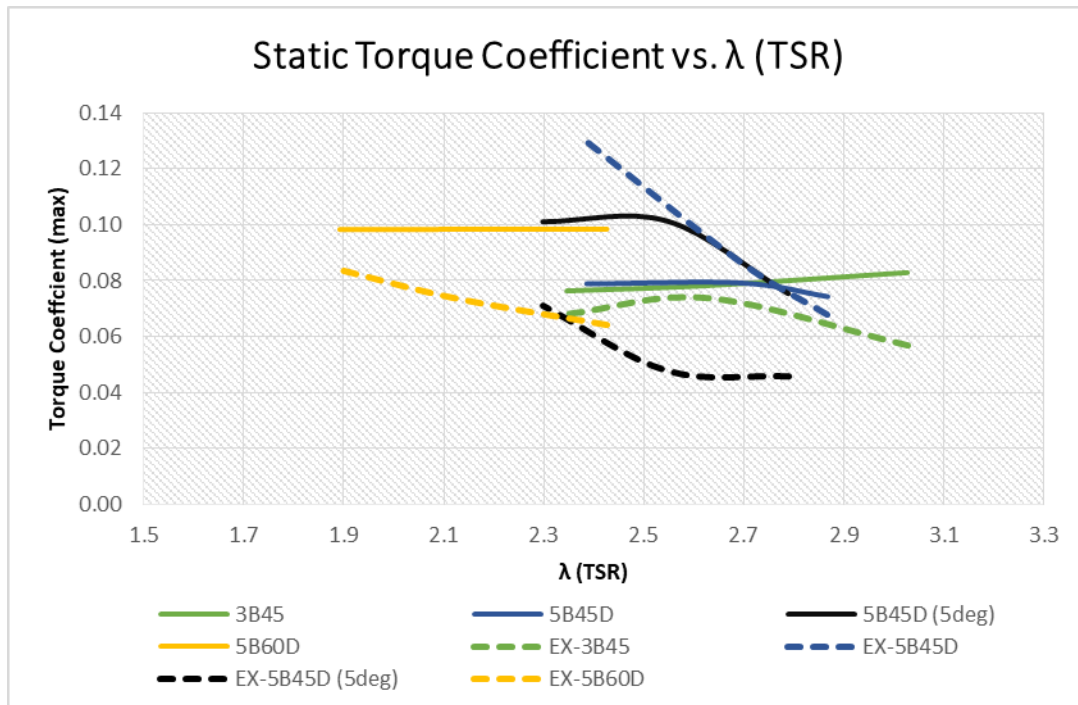
Figure 4.29. Torque Coefficient vs. TSR.
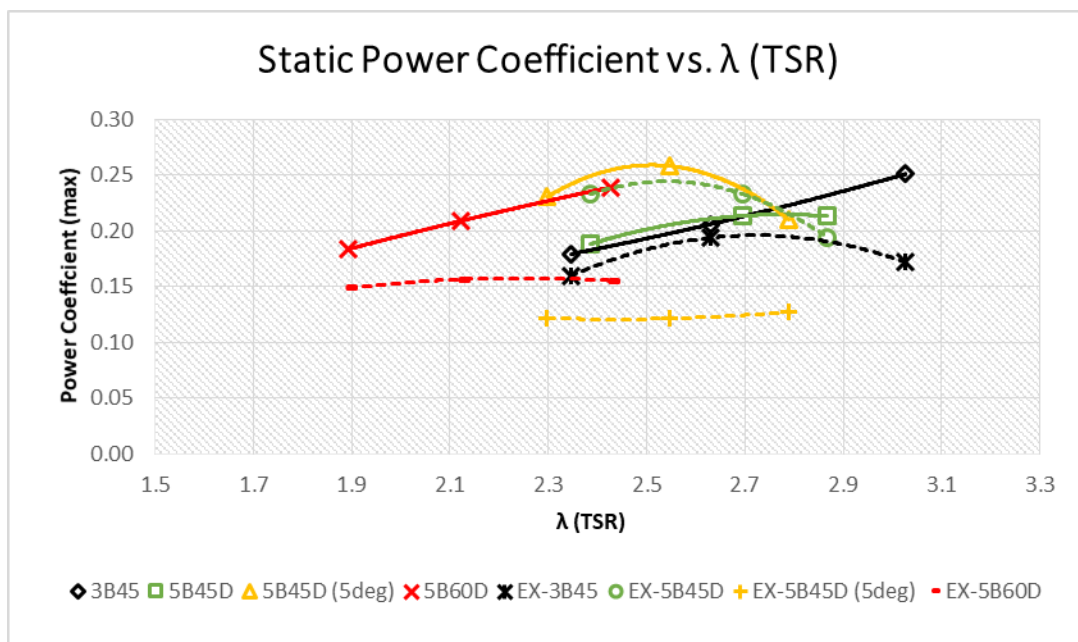
Figure 4.30. Power Coefficient vs. TSR.

From Figure 4.29 and Figure 4.30, it can be observed that the data had relatively good agreement both numerically and experimentally with the exception of the 5B45 (5deg) rotor

assembly, which, exhibited a very dramatic incoherence with the experimental and theoretical data. The TSR values ranged from 1.89 to 3.03. One thing that did remain true for both experimental and numerical tests however is that the 5B60D rotor preferred a lower operating TSR than the other rotor models.

It should be noted that all numerical results are being assessed after about 5 seconds of rotation and all experimental results are assessed after 120 seconds of rotation. The values represented were only done for wind speeds of 8, 10 and 12 m/s and were plotted from the max values of the torque and power coefficients.

4.4.2 Pressures and Velocities

The pressures and velocities surrounding the blades during Static Numerical analysis for each rotor, are closely observed at the time step 300 while each turbine was at the zero degree azimuth position. CFD post-processing within the ANSYS CFX software is used to investigate the aerodynamic characteristics at this time step in each rotor. Air pressure contours surrounding the blades, air velocity vectors, and blade wall pressures are displayed in Figure 4.31 to Figure 4.34 at 12 m/s wind velocity.
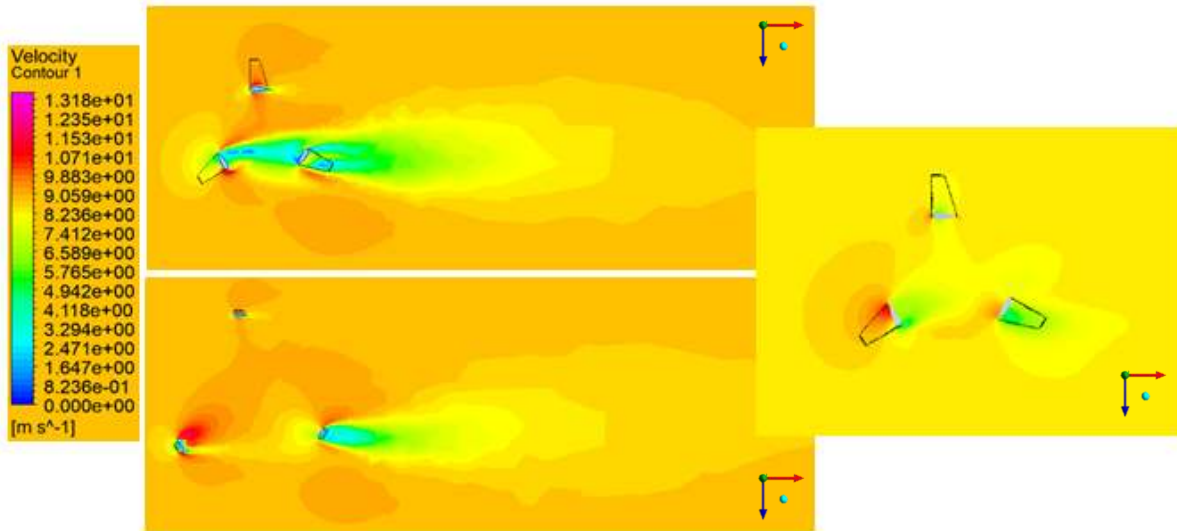
Figure 4.31. 3B45D Velocity and Pressure Contours @12m/s.
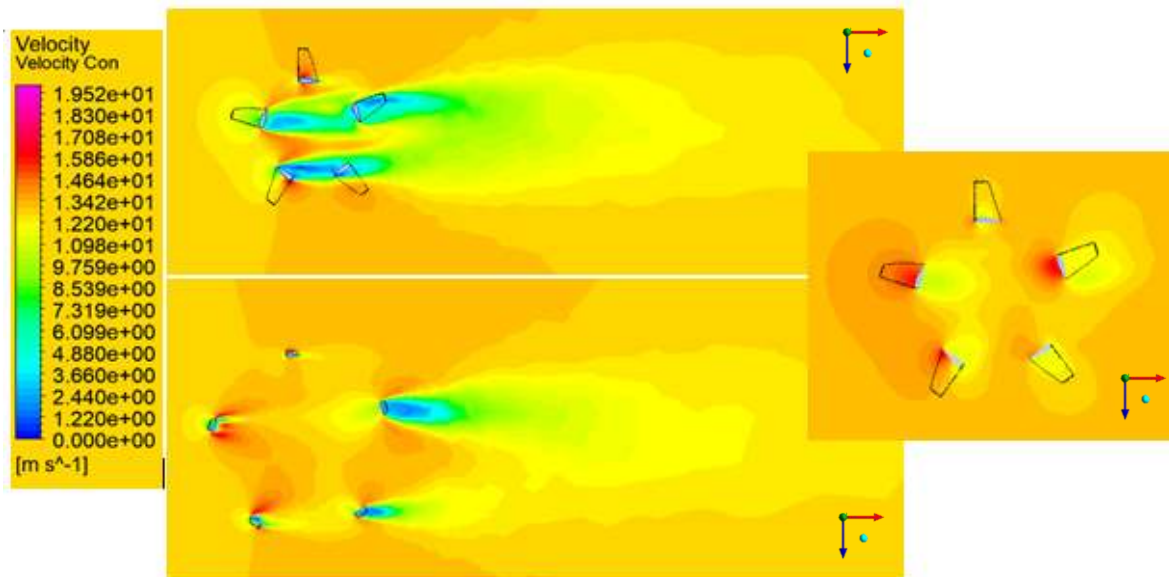
Figure 4.32. 5B45D Velocity and Pressure Contours @12m/s.

In all the models depicted, higher air velocities are present at the tips of the blades. The rotor geometries with a higher number of blades prevent more wind from passing through the turbines rotors center; as a result it can be noticed that there is a larger area of de-energized air behind the turbines with more blades than those with less blades. This translates to the pressures surrounding rotor models with higher number of blades being much higher, with an area of lower pressure in

the center of these rotors. This is one of the effects that solidity can have on a rotor. It is important to note that the effects depicted here are under static rotor conditions.

Observe carefully as well the velocities around the blades of models with a higher number of blades are faster, with velocities around these rotor model blades from a 12m/s breeze reaching as high as 20.59m/s in the 5B60D (Figure 4.34) rotor model.
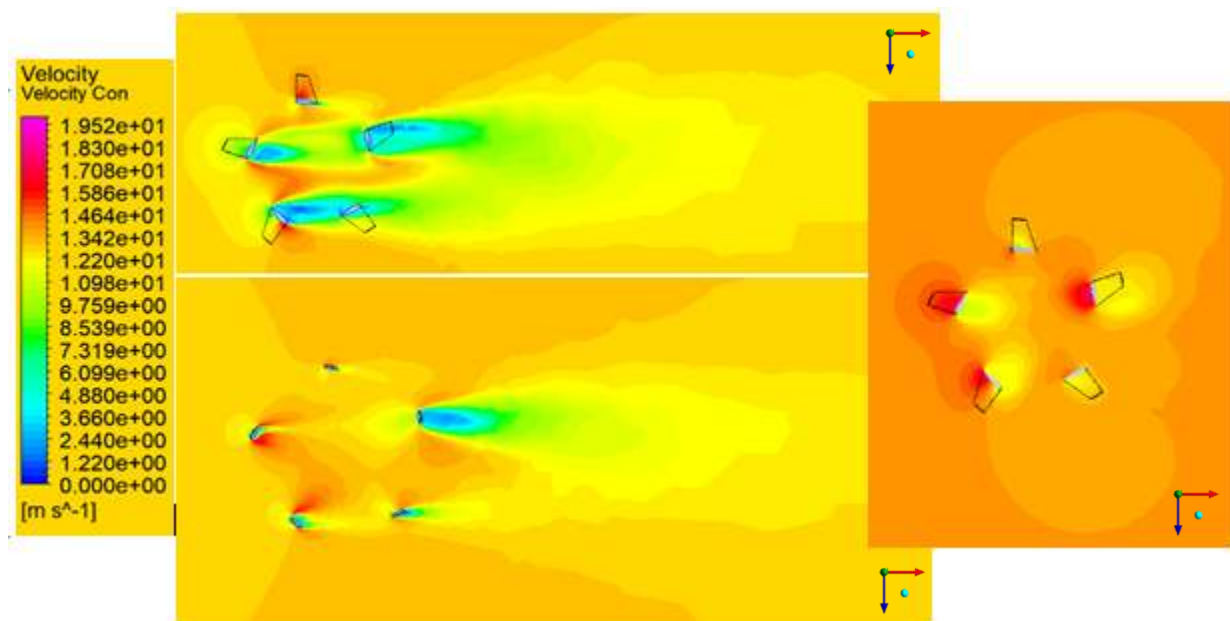
Figure 4.33. 5B45D (5deg) Velocity and Pressure Contours @12m/s.

The blades which are upwind facing the wind in a flapwise manner are experiencing drag, while the blades upwind facing the wind in an edgewise direction are experiencing lift. In each figure there can be seen behind each upwind blade experiencing drag, an area of de-energized wind.
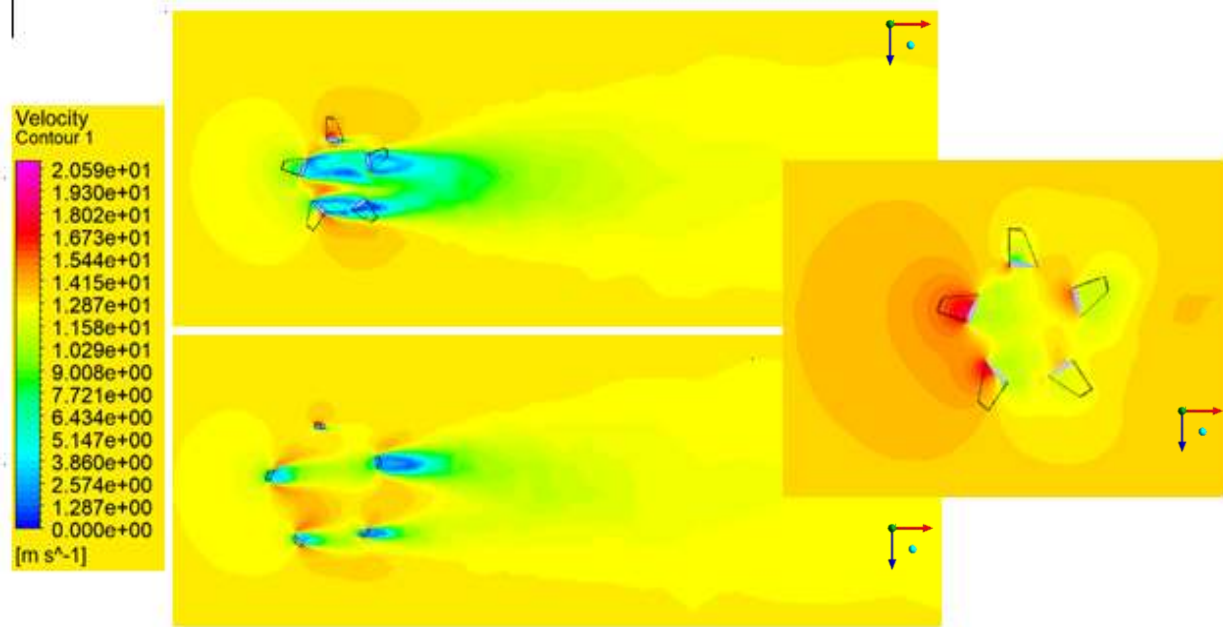
Figure 4.34. 5B60D Velocity and Pressure Contours @12m/s.

The de-energized wind coming from these blades passes through the center of the turbine to the blades downwind. This effect blocks the wind from the downwind blades. This effect is what caused the structural catastrophes in the work done by (Veers 1981). In each rotor assembly it can be seen where each blade will experience, at least 3 cycles of flapwise fatigue loading and 2 cycles of edgewise fatigue load during operation. This is the reason fatigue analysis for VAWT is of such great importance.

4.4.3 Transient Aerodynamic Results

The transient analysis was carried out as expressed in Chapter 3 of this document. The results are detailed here. The transient analysis began with experimental testing in order to establish the boundary conditions for the transient numerical study. One of these preliminary parameters is expressed in RPM measurements which were taken as was described previously in Chapter 3. The gathered experimental data was translated to angular velocity and is represented in

Figure 4.35. Note that the data depicted in Figure 4.35 was also used in the determination of the static aerodynamic study as well.
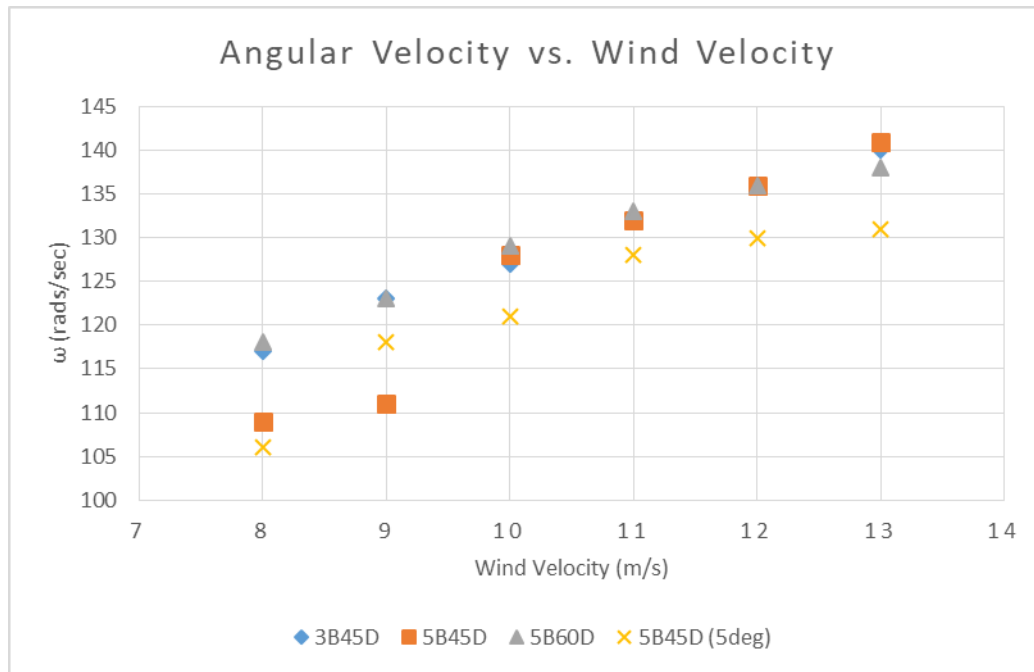
Figure 4.35. Experimental angular velocity vs wind velocity.

The summary of the collected data depicted in Figure 4.35, illustrates 5B45D (5deg) turbine rotor has the lowest angular velocity at 8 m/s followed by the 5B45D rotor. The 3B45D and the 5B60D rotor model exhibited a superior angular velocity at the start of the wind range, but is, however, matched by the 5B45D design from 10 m/s onwards. The 5B45D (5deg) maintained consistently the lowest angular velocity throughout the tested wind range except for at 9 m/s.

It should be noted that there is no load on the turbine as it rotates. The results of this transient performance, are from freely rotating rotors. This was done in an effort to keep the data consistent from numerical analysis to experimental whether static or transient dynamic.

Table 4.6, depicts a summary of transient dynamic results for both experimental and numerical study. The data again only displays 8, 10 and 12 m/s wind speeds.

Experimental				
Rotor	**TSR**	**V (m/s)**	**C_p**	**C_m**
EX-3B45D	**3.027375**	**8**	**0.039876**	**0.013172**
	2.6289	**10**	**0.096781**	**0.036814**
	2.346	**12**	**0.123038**	**0.052446**
EX-5B45D	**2.868063**	**8**	**0.042015**	**0.014649**
	2.6944	**10**	**0.096204**	**0.035705**
	2.385667	**12**	**0.155942**	**0.065366**
EX-5B45D (5deg)	**2.789125**	**8**	**0.007351**	**0.002636**
	2.54705	**10**	**0.032382**	**0.012713**
	2.297958	**12**	**0.044139**	**0.019208**
EX-5B60D	**2.426375**	**8**	**0.027429**	**0.011305**
	2.12205	**10**	**0.065524**	**0.030878**
	1.89175	**12**	**0.071099**	**0.037584**
Numerical				
Rotor	**TSR**	**V (m/s)**	**C_p**	**C_m**
3B45D	**3.027375**	**8**	**0.067535**	**0.022308**
	2.6289	**10**	**0.097997**	**0.037277**
	2.346	**12**	**0.057702**	**0.024596**
5B45D	**2.868063**	**8**	**0.259812**	**0.090588**
	2.6944	**10**	**0.187366**	**0.069539**
	2.385667	**12**	**0.129399**	**0.05424**
5B45D (5deg)	**2.789125**	**8**	**0.019051**	**0.006831**
	2.54705	**10**	**0.015716**	**0.00617**
	2.297958	**12**	**0.021047**	**0.009159**
5B60D	**2.426375**	**8**	**0.099177**	**0.040315**
	2.12205	**10**	**0.088115**	**0.040955**
	1.89175	**12**	**0.075442**	**0.039912**

Table 4.6. Transient Results Summary.

From Table 4.6, we gather that the maximum transient value of C_p that was obtained is 0.259, achieved by the 5 bladed 45 degree rotor numerically at a TSR of 2.87. By comparison, this experimental power coefficient value at the same TSR was 0.042, which shows a very large percent difference. Figure 4.36 graphically summarizes the data expressed in Table 4.6.

In Figure 4.36, the transient numerical vs transient experimental power coefficient is displayed as a function of TSR. As can be identified from the figures, the data coincides, however, there are instances where the experimental set-up is performing better than the numerical model. There are also large discrepancies in the data, especially with the 5B45D rotor model. This would suggest that either the numerical setup is too conservative or the experimental setup has inconsistencies.

Figure 4.36. Transient Power Coefficient vs. TSR.
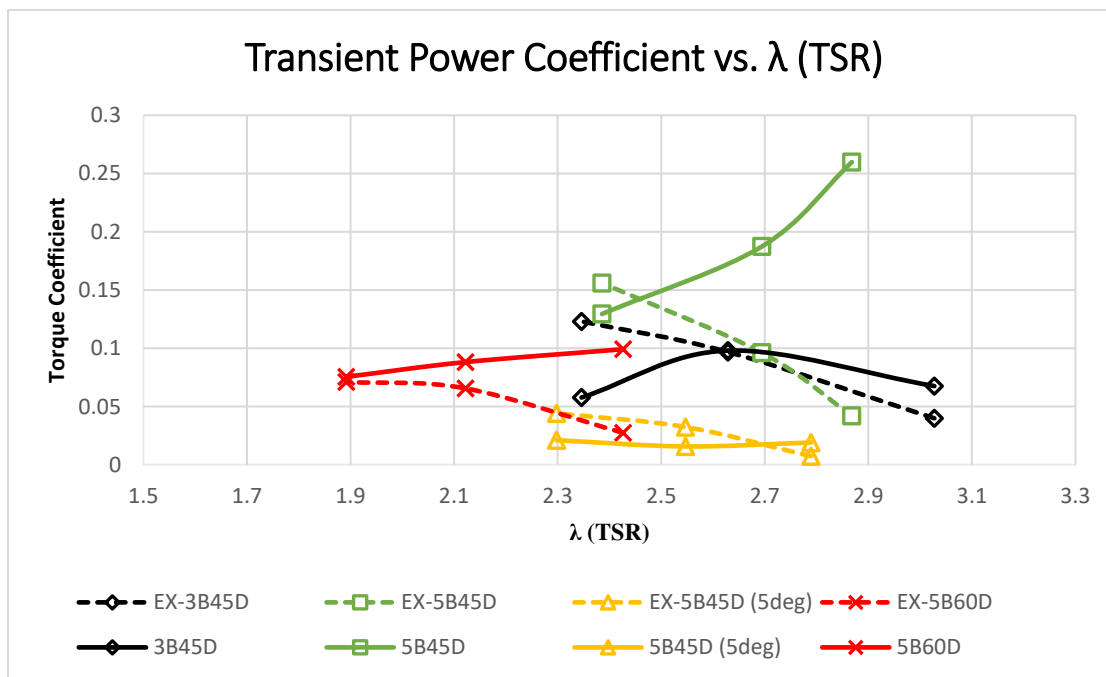
It should be noted that throughout this work, the 3B45D rotor has given excellent agreement in both experimental and numerical testing. The difference in the obtained efficiencies can be attributed to the transient study being conducted under load versus values collected in the static portion of the study, which are theoretically calculated from obtained torque measurements.

CHAPTER 5

CONCLUSION

5.1 Summary of Work

The work carried out in this project sought to investigate the structural and aerodynamic characteristics of a relatively understudied, rotor type. Through the use of numerical and experimental efforts the aerodynamic performances as well as structural responses have been assessed. Three different models are used in the structural study and 4 in the aerodynamic study. The use of ANSYS 19.1 analysis software was applied in order to simulate the effects of wind on proposed rotor configuration. Additive manufacturing was then employed to fabricate geometries that were used in experimental testing.

ANSYS CFD simulations are performed to validate the structural design as well as aerodynamic characteristics for the new V-shaped rotor. Torque as well as power Performance coefficients of each tested model is determined from wind tunnel experimentation, after which, experimental data is then used for input boundary conditions of the 3D numerical simulations.

5.2 Rationale for Discrepancies

The numerical data obtained from both structural and aerodynamic study is of satisfactory cohesiveness. The experimental and numerical data from the aerodynamic portion of this study, however, did not coincide with. This observation is clear from the observed data. The numerical efforts of this study is believed to be correct based on the methods applied and laid out by, (IEC TC 88 2006), (FLUENT 2012) and (Kishore 2013). The discrepancies, it is believed, arose from issues having to do with the experimental set-up. The following reasons are cited as probable causes for the lack of cohesiveness between experimental and numerical data:

- Blades from the additive manufacturing were warped and caused unstable rotation of the wind turbine rotor models. This there caused the models to vibrate, thereby affecting torque measurements.

- The hub used for the experimental set-up was too heavy/robust for rotor designs under study.

- The designed lock shaft mechanism used to measure static torque was designed using ABS plastic. This material proved to be unsuitable and cause a wobbling motion during static measurement. This vibration could have led to incorrect reading during experimental static torque testing.

These reasons are plausible since we do not observe the same patterns in the experimental torque data as we do in the numerical torque data, such as number of peaks coinciding with number of blades on the rotor.

5.3 Conclusions

The conclusions drawn from this study are as follows:

- In accordance with IEC wind turbine design codes, the chosen blade geometry and subsequent rotor assembly was structurally safe enough to run physical tests.

- The blade geometry of blade design 2 out did all other models in every criteria. Therefore it was chosen for aerodynamic study.

- The redesigned rotor design has a fatigue loading FOS of 1.87 for a wind speed of 8m/s and a resulting life of 1.02E+10 hours. While the blade showed a life of 1.76E+10 hours and a FOS is 2.29. This corresponded to a difference of ~20% in FOS. The achieved FOS was higher than the set criteria of FOS greater than or equal to 1.5.

- Highest average power coefficient observed in the study was 0.258. It was obtained numerically by the 5-bladed rotor with a 45 degree incline and a 5 degree blade twist (5B45D (5deg)) at a TSR of 2.54.

- The rotors operate between a TSR of 1.8 and 3.03, with the 60 degree inclined rotor (5B60D) performing at a lower TSR than the other rotors which had a 45 degree incline.

- The 3 bladed 45 degree (3B45D) rotor produces the second highest power coefficient of 0.251 at a TSR of 3.03 and was the rotor assembly that gave best agreement with both numerical and experimental results.

- In terms of consistency in the data, the 3B45D performed the most consistent with power coefficient values of:

  Static Simulation 0.206; Static Experimental 0.194 both at TSR = 2.63 which is ~6% difference.

- The 3 bladed 45 degree rotor assembly wider covered the widest range of TSR.

- The numerical conclusions achieved by this study are validated and accepted, while the experimental values obtained require more careful study to be reliable.

- Experimental methods need to be assessed and improved.

REFERENCES

Abu-El-Yazied, Taher G., Ahmad M. Ali, Mahdi S. Al-Ajmi, and Islam M. Hassan. 2015. "Effect of Number of Blades and Blade Chord Length on the Performance of Darrieus Wind Turbine." *American Journal of Mechanical Engineering and Automation* 16-25.

Alaimo, Andrea, Antonio Esposito, Antonio Messineo, Calogero Orlando, and Davide Tumino. 2015. "3D CFD Analysis of a Vertical Axis Wind Turbine." *Energies (19961073)* 3013-3033.

AWS True Power. n.d. *Georgia Wind Resource Map at 30 Meters.* Accessed October 5, 2018. https://windexchange.energy.gov/maps-data/160.

Barnes, R.H., E.V. Morozov, and K. Shankar. 2015. "Improved methodology for design of low wind speed specific wind turbine blades." *Composite Structures* 119: 677-684.

Bashar, Mohammad M., Mosfequr Rahman, and Khan. 2014. *Computational and Experimental Study on Vertical Axis Wind Turbine in Search for an Efficient Design.* Thesis, Statesboro: Georgia Southern University College of Graduate Studies (GSU COGS).

Beckford, Tosha . 2017. *Wind turbines provide 8% of U.S. generating capacity, more than any other renewable source.* Technical Report, Washington D.C.: U.S. Energy Information Administration (EIA).

Bourell, D. 2017. "Materials for Additive Manufacturing." *Manufacturing Engineering* 659.

Browell, Raymond, and Al Hancq. 2006. "Calculating and Displaying Fatigue Results." *ANSYS Support.* March 29. Accessed October 5, 2018. https://support.ansys.com/staticassets/ANSYS/staticassets/resourcelibrary/whitepaper/fatigue.pdf.

Brown, Matthew. 2016. *Vertical Axis Wind Turbines.* December 13. Accessed October 5, 2018. http://large.stanford.edu/courses/2016/ph240/brown2/.

Bureau of Labor Statistics. 2018. *Wind Turbine Technicians.* Washington, D.C., April 13.

Caliskan, Samet, A Ş Com, Farba Karaca Ahmet, and Ali. Yildiz. 2016. "Fatigue properties of ABS Thermoplastics used in exterior lighting." *Manufacturing Engineering.*

Castelli, Marco Raciti, Stefano De Betta, and Ernesto Benini. 2012. "Effect of Blade Number on a Straight-Bladed Vertical-Axis Darreius Wind Turbine." *World Academy of Science, Engineering and Technology International Journal of Aerospace and Mechanical Engineering* 6 (1): 68-74.

Chougule, Prasad, and Søren Nielsen. 2014. "Overview and Design of self-acting pitch control mechanism for vertical axis wind turbine using multi-body simulation approach." *Journal of Physics.*

Dabiri, John O. 2011. "Potential order-of-magnitude enhancement of wind farm power density via counter-rotating vertical-axis wind turbine arrays." *Journal of Renewable and Sustainable Energy* 3 (4).

Dominy, R., P. Lunt, A. Bickerdyke, and J. Dominy. 2007. "Self-starting capability of a Darrieus turbine." *MECH E part A : Journal of power and energy.* Durham: Durham University. 110-120.

Elliot, D.L., L.L. Wendell, and G.L. Gower. 1991. *An Assessment of the Available Windy Land Area and Wind Energy Potential in the Contiguous United States.* PhD Thesis, Richland: U.S. Department of Energy.

F2792 −12a, ASTM International. 2013. "Standard Terminology for Additive Manufacturing Technologies F2792 − 12a."

FLUENT. 2012. "ANSYS Release Version 15.0 User's Guide." Canonsburg, PA: ANSYS Inc.

Hussen, MD. Saddam, Dr. K. Rambabu, M. Ramji, and E. Srinivas. 2015. "Design and Analysis of Vertical Axis Wind Turbine Rotors." *International Journal on Recent Technologies in Mechanical and Electrical Engineering (IJRMEE)* 2 (9): 54-62.

IEC TC 88. 2006. *Wind turbines — Part 2: Design requirements for small wind turbines EN 61400-2:2006.* Standard, BSI.

Ilas, Andrei, Pablo Ralon, Asis Rodriguez, and Michael Taylor. 2018. *Renewable Power Generation Costs in 2017.* Annual Publication, Abu Dhabi: International Renewable Energy Agency (IRENA).

Ju, Dayuan, and Qiao Sun. 2017. "Modeling of a Wind Turbine Rotor Blade System." *ASME Journal of Vibration and Acoustics* 139 (5).

Kishore, Ravi Anant. 2013. *Small-scale Wind Energy Portable Turbine (SWEPT).* Thesis, Blacksburg: Virginia Polytechnic Institute and State University.

Kjellin, J., F. Bülow, Sandra Eriksson, P. Deglaire, Mats Leijon, and Hans Bernhoff. 2011. "Power coefficient measurement on a 12 kW straight bladed vertical axis wind turbine." *Renewable Energy* 3050-3053.

Kumar, Rajesh, and Prashant Baredar. 2014. "Solidity Study and its Effects on the Performance of A Small Scale Horizontal Axis Wind Turbine." *Impending Power Demand and Innovative Energy Paths* 290-297.

Kusnetz, Nicholas. 2018. "4 States Get Over 30 Percent of Power from Wind — and All Lean Republican." *Inside Climate News*, April 20.

Lee, Huei-Huang. 2017. *Finite Element Simulations with ANSYS Workbench 17: Theory, Applications, Case Studies.* Mission: SDC Publications.

Li, Qing'an, Takao Maeda, Yasunari Kamada, Junsuke Murata, Kento Shimizu, Tatsuhiko Ogasawara, Alisa Nakai, and Takuji Kasuya. 2016. "Effect of solidity on aerodynamic

forces around straight-bladed vertical axis wind turbine by wind tunnel experiments (depending on number of blades)." *Renewable Energy* 96: 928-939.

Li, Qing'an, Takao Maeda, Yasunari Kamada, Kento Shimizu, Tatsuhiko Ogasawara, Alisa Nakai, and Takuji Kasuya. 2017. "Effect of rotor aspect ratio and solidity on a straight-bladed vertical axis wind turbine in three-dimensional analysis by the panel method." *ENERGY* 121: 1-9.

Li, Rennian, and Xin Wang. 2011. "Status and challenges for offshore wind energy." *International Conference on Materials for Renewable Energy & Environment.* Shanghai: IEEE. 601-605.

Li, Shengmao., and Yan. Li. 2010. "Numerical study on the performance effects of solidity on the straight-bladed vertical axis wind turbine." *Asia-Pacific power and energy engineering conference.* Chengdu: IEEE.

MacPhee, David, and Asfaw Beyene. 2012. "Recent Advances in Rotor Design of Vertical Axis Wind Turbines." *Wind Engineering* 36 (6): 647-666.

Mahesh, Aeidapu , and Kanwarjit Singh Sandhu. 2015. "Hybrid wind/photovoltaic energy system developments: Critical review and findings." *Renewable and Sustainable Energy Reviews* 52: 1135-1147.

Manwell, J. F., J. G. McGowan, and A. L. Rogers. 2009. *WIND ENERGY EXPLAINED: Theory, Design and Application.* 2. West Sussex: John Wiley & Sons Ltd.,.

Marín, J.C., A. Barroso, F. París, and J.Cañas. 2009. "Study of fatigue damage in wind turbine blades." *Engineering Failure Analysis*, March: 656-668.

Newegg.com. n.d. *Newegg.* Accessed October 2, 2018. https://www.newegg.com/Product/Product.aspx?Item=152-000N-00046.

Osea, Vola, and Eqwan M.Roslan. 2017. "Study on Wind Speed Correlation between UNITEN and Meteorological Station Data for Wind Resource Assessment." *International Journal of Scientific Research in Science, Engineering and Technology* 3 (5): 372-378.

Owens, B. C., and D. T. Griffith. 2014. "Aeroelastic Stability Investigations for Large-scale Vertical Axis Wind Turbines." *Journal of Physics.* IOP Publishing Ltd.

Owens, B. C., and D. T. Griffith. 2015. "Aeroelastic Stability Investigations for Large-scale Vertical Axis Wind Turbines." *Journal of Physics: Conference Series 524.* IOP Publishing Ltd.

Parra, Teresa, Carmen Vega, Gallegos A., Uzarraga N.C., and Castro F. 2014. "Design of a H-Darreius Vertical Axis Wind Turbine." 1-4.

Parsons, D.J., J.C. Chatterton, F.P. Brennan, and A.J. Kolios. 2011. *Novel Offshore Vertical Axis Wind Turbines.* Case Study, Cranfield University.

Perry, Dylan. 2015. *AERODYNAMIC DESIGN AND STRUCTURAL ANALYSIS PROCEDURE FOR SMALL HORIZONTAL-AXIS WIND TURBINE ROTOR BLADE.* Thesis, California: California Polytechnic State University.

Rezaeiha, A., I. Kalkman, and B. Blocken. 2017. "Effect of pitch angle on power performance and aerodynamics of a vertical axis wind turbine." *Applied Energy* 132-150.

Roscher, B. 2014. *Structural Optimization Of A Vertical Axis Wind Turbine With Aeroelastic Analysis.* Masters Thesis, Delft: Technical University of Denmark, Department of Wind Energy.

Salyers, Travis E. 2016. "Experimental and Numerical Investigation of Aerodynamic Performance for Vertical-Axis Wind Turbine Models with Various Blade Designs." Masters Thesis, Department of Mechanical Engineering, Georgia Southern University, Statsboro.

Schwabe, Paul, Sander Lensink, and Maurine Hand. 2011. *IEA Wind Task 26: Multi-national Case Study of theFinancial Cost of Wind Energy.* National Renewable Energy Laboratory Technical Report, Golden: National Renewable Energy Laboratory (NREL).

Sellami, Takwa, Hanen Berriri, A. Moumen Darcherif, Sana Jelassi, and M. Faouizi Mimouni. 2016. "Modal and harmonic analysis of three-dimensional wind turbine models." *Wind Engineering* 40 (6): 518-527.

Sharpe, David John. 2011. Vertical Axis Turbine Aparatus. USA Patent US8038383B2. 10 18.

Shires, Andrew. 2013. "Development and Evaluation of an Aerodynamic Model for a Novel Vertical Axis Wind Turbine Concept." *Energies* 2501-2520.

Staino, Andrea, and Biswajit Basu. 2015. "Emerging trends in vibration control of wind turbines: A focus on a dual control strategy." *Philosophical Transactions of the Royal Society A: Mathematical, Physical, and Engineering Sciences*, 373.

Sun, Xiaojing, Yajun Chen, Yang Cao, Guoqing Wu, Zhongquan Zheng, and Diangui Huang. 2016. "Research on the aerodynamic characteristics of a lift drag hybrid vertical axis wind turbine." *Advances in Mechanical Engineering* 8 (1).

Sutherland, Herbert J., Dale E. Berg, and Thomas D. Ashwill. 2012. *A Retrospective of VAWT Technology.* Research Study, Albuquerque: Sandia National Laboratories.

Tawade, Satishkumar V., Sachin B. Todkar, and Ashwinikumar S. Hade. 2014. "FATIGUE LIFE OPTIMIZATION OF WIND TURBINE BLADE." *International Journal of Research in Engineering and Technology (IJRET)* 3 (3): 843-850.

Vaughan, Adam. 2017. "Mersey feat: world's biggest wind turbines go online near Liverpool." *The Guardian*, May 17.

Veers, Paul S. 1981. *Approach to Fatigue Analysis of Vertical Axis Wind Turbine Blades.* Technical Report, Albuquerque: Sandia National Laboratories, 5-9.

Vernier Software & Technology. n.d. *Solidity.* Accessed October 5, 2018. https://www.vernier.com/experiments/rev/11/solidity/.

Wang, Lin, Athanasios Kolios, Takafumi Nishino, Pierre-Luc Delafin, and Theodore Bird. 2016. "Structural Optimization of Vertical Axis Wind Turbine Composite Blades Based on Finite Element Analysis and Genetic Algorithm." *Composite Structures* 153: 123-138.

Windy Nation. 2010. *Tip Speed Ratio: How to Calculate and Apply TSR to Blade Selection.* September 12. Accessed October 23, 2018. https://www.windynation.com/cm/wind_tip-speed-ratio-how-calculate-and-apply-tsr-blade-selection.pdf.

Xfoil. n.d. *Xfoil Prediction Polar: NACA 4 Digit Airfoil Generator.* Accessed December 12, 2017. http://airfoiltools.com/polar/details?polar=xf-naca0015-il-50000.

Xie, Shengbai, Cristina L. Archer, Niranjan Ghaisas, and Charles Meneveau. 2016. "Benefits of collocating vertical-axis and horizontal-axis wind turbines in large wind farms." *Wind Energy.*